Nonclassical magnon pair generation and Cauchy-Schwarz inequality violation

Yaqi Fan,[*] Jiahua Li [ORCID],[†] and Ying Wu[‡]

School of Physics, Huazhong University of Science and Technology, Wuhan 430074, People's Republic of China

We theoretically propose a magnon-based superconducting qubit hybrid system containing two ferromagnetic yttrium iron garnets (YIGs) and one superconducting qubit, demonstrating that this hybrid quantum system is feasible in achieving the unconventional two-mode magnon blockade and generating the quantum correlated magnon pairs. Through the virtual-photon excitation mediated by the same cavity mode, the effective couplings can be established not only between the Kittel modes and the qubit, but also between the two Kittel modes. We characterize the magnon blockade by utilizing the equal-time second-order correlation functions and impose a constraint on the correlations between the two Kittel modes by introducing the Cauchy-Schwarz inequality (CSI). In the weak qubit-magnon coupling regime, our results indicate the following: (i) Under the scenario of the resonance couplings, the ratio of driving strengths and the ratio of coupling strengths between the two Kittel modes and the cavity mode can be employed to control and regulate the magnon blockade and the violation of the CSI. Not only the two Kittel modes can achieve the unconventional magnon antibunching effects simultaneously, but also the correlations between them violate the classical CSI. It is important to note that when the degrees of both the antibunching effects for the two Kittel modes and the anticorrelation between them reach their highest levels simultaneously, the correlations happen not to violate the CSI. But our proposal offers a feasible route for preparing a high-quality single-magnon source. (ii) Under the scenario of the out-of-resonance couplings, by adjusting the frequency detunings between the first Kittel mode and the second Kittel mode as well as the qubit, the quantum correlated two-mode magnon pairs can be obtained. (iii) Finally, it is found that the magnon antibunching effect of the second Kittel mode is robust against the dissipation ratio between the two Kittel modes. These results illustrate how to optimally choose the parameters to realize nonclassical magnon pair generation and CSI violation. The hybrid YIG quantum system we propose here holds the potential in the development of efficient microwave single-magnon sources and quantum magnon-magnon pairs required in future quantum information processing tasks.

I. INTRODUCTION

As a promising platform for exploring intriguing quantum optical phenomena, hybrid quantum systems based on magnonics [1–3] have attracted great research attention. Yttrium iron garnet (YIG) [4,5], a ferromagnetic material with great potential in the field of quantum information, is often utilized to construct new hybrid quantum systems by combining it with various physical systems due to its small mode volume [6,7], low dissipation rate [5,8,9], high spin density [8,10,11], and high Curie temperature [11,12]. Magnon, which is the collective spin-excited quanta in YIG [3,6,13,14], has potential value to be employed as a novel logic device for carrying and processing information. For example, (i) through the magnetostrictive interaction, the magnon modes can be coupled to the mechanical modes in the cavity magnomechanics [3,15–17]; (ii) through the magneto-optical effect, i.e., the Faraday effect, the magnon modes can be coupled to the optical cavity mode in the cavity optomagnonics [18,19]; and (iii) through the magnetic dipole interaction, the magnon modes

can be coupled to the microwave cavity mode in the cavity electromagnonics [5,8,11]. Based on the above available physical basis, many interesting quantum phenomena involving magnons have been reported, such as the generation of the quantum squeezed states of magnons and phonons [15], the magnetically controllable slow light [16], the magnon-photon-phonon tripartite entanglement [17], the magnon dark modes [20,21], the magnon blockade effect [22–25], and so on.

In a ferromagnetic sphere, there are numerous magnetostatic modes which are called Walker modes [1,26–28]. In the microwave magnetic field which is uniform throughout the ferromagnetic sample, the YIG sphere possesses uniform spin precession [13,29], then the magnetic dipole couplings of the nonuniform magnetostatic modes disappear [1]. As a result, the uniform magnetostatic mode, i.e., the Kittel mode which is the simplest Walker mode, becomes the dominant coupled magnetostatic mode [1,13]. Again, due to the nonlinear natures of Josephson junction, the superconducting qubit is admitted as an artificial two-level atom in various hybrid systems [29–31]. In a hybrid ferromagnet-superconductor quantum system, the effectiveness of the indirect coupling between the superconducting qubit and the Kittel mode in the spin ensembles has been experimentally recognized [13,26,29,32]. And by utilizing superconducting qubit as an aid, there are experiments which have demonstrated how

[*]yaqi_fan2023@126.com
[†]Corresponding author: huajia_li@163.com
[‡]yingwu2@126.com

to detect a single magnon [33], and generate the quantum states of the magnon and achieve precise quantum control of a single magnon [34]. These experimental backgrounds provide us with a viable option and an available platform to study the quantum phenomena of the magnon. Based on the understanding and study of the photon blockade [35–37] and the phonon blockade [38–41], the magnon blockade has been theoretically proposed for the first time as a pure quantum effect [22]. It describes a pure quantum effect based on magnons: after the transmission of the first magnon, the transmission of the second one will be suppressed, indicating that the magnon statistical characteristics follow the sub-Poisson distribution [23]. This nonclassical effect based on magnons facilitates the preparation of a single-magnon source and makes the operation at the level of a single magnon to be possible, which serves as an important component of the quantum information science. According to different blockade generation mechanisms, the magnon blockade effect can be classified into two cases. The first case of the magnon blockade effect requires that there are strong nonlinear interactions between the magnon modes and the qubit, which result in the anharmonicity of the dressed states in the hybrid quantum system [25,32,42], and this magnon blockade effect is defined as the conventional magnon blockade effect [22,23] similar to the conventional (nonlinearity-mediated) photon blockade [37,43]. The second case of the magnon blockade effect can be achieved under the condition of weak nonlinear interactions which allow us to utilize the destructive quantum interference between different transition pathways to realize the unconventional magnon blockade [23,25,42,44–46] similar to the unconventional (interference-mediated) photon blockade [37,47,48]. The second-order correlation function [49] needs to be introduced to characterize this nonclassical effect. For a hybrid quantum system containing multiple modes, one can employ the second-order autocorrelation function to investigate the degree of the excitation competition between the same mode. In addition, one can employ the second-order cross-correlation function to investigate the correlations between different modes. For example, in the quantum system with two phonon modes [50,51], two photon modes [52,53], the mixed modes of the phonon mode and the photon mode [54–56], and the mixed modes of the photon mode, the Kittel mode, and the phonon mode [57], the correlations between different modes can be quantified by exploiting the second-order cross-correlation function which needs to be bounded by the classical inequalities.

As a fundamental multimode inequality, the classical Cauchy-Schwarz inequality (CSI) [58,59] provides an important mathematical tool for the research of quantum optics. It can be used to explore the nonclassical properties of the correlations between different modes [54,58–63]. The classical CSI imposes a constraint on the correlations between different modes [62], whose violation is a nonclassical behavioral feature and ranks among the major evidence for the presence of the nonclassical correlations between different modes. The violation of the classical CSI was first experimentally demonstrated in the atomic two-photon cascade radiation in the 1970s by Clauser [64]. In addition, it can be used to study the nonclassical property of the two-photon pairs generated from the collective emission in an atomic ensemble [65], the

second harmonic [66], and optical four-wave mixing [67–69]. It can also be used to prove the existence of the entanglement in a many-body system [70].

Inspired by existing advances involving the magnon blockade effect [22–25,42,44–46,71,72], we consider a hybrid quantum system consisting of two YIG spheres and one superconducting qubit. The introduction of an additional YIG sphere provides more nonlinearities that can be exploited to explore the quantum phenomena. Because the qubit and the two Kittel modes are coupled to the same cavity mode, the effective couplings can be established not only between the two Kittel modes and the qubit, respectively, but also between the two Kittel modes through the virtual-photon excitation. We drive the two Kittel modes with the same driving frequency. We can adjust the system parameters, such as the ratio of coupling strengths, the ratio of driving strengths, the driving detuning, the frequency detuning between the two Kittel modes, the frequency detuning between the first Kittel mode and the qubit, the qubit dissipation, and the dissipation ratio between the two Kittel modes, to modulate and control the magnon blockade effects characterized by the equal-time second-order autocorrelation functions. It should be noted that the coupling strengths we adjust here are those between the Kittel modes and the cavity mode, rather than the effective coupling strengths between the qubit and the two Kittel modes. Since the hybrid quantum system we consider contains two Kittel modes, we introduce the equal-time second-order cross-correlation function to determine whether there are excitation competitions between them. Finally, we introduce the CSI which can associate the two equal-time second-order autocorrelation functions with the equal-time second-order cross-correlation function to determine whether there are quantum correlations between different modes. Also, we provide an approximate analysis which yields further physical insight into the numerical results. Our study has potential applications in preparing efficient microwave single-magnon sources and microwave two-magnon gateways for quantum communication in sophisticated quantum network architectures.

It should be pointed out that previous works [71,73] also additionally introduce a YIG sphere, but the magnon blockade effects of the two Kittel modes are not fully explored, and the systemic study of the quantum properties of the correlations between them are also missing. Compared with the previous works [71,73], our proposal provides more complete information for the hybrid ferromagnet-superconductor quantum system containing multiple YIG spheres to realize the two-mode magnon blockade effects and the two-magnon gateways based on a very different operation condition. To be more specific, several remarks are in order.

(i) Previous works involving two YIG spheres [71,73] or two qubits [23] use two mutually perpendicular microwave cavities, and thus only establish effective qubit-magnon couplings but not effective magnon-magnon or qubit-qubit coupling. Unlike Refs. [71,73], our proposal establishes the effective tripartite couplings among the two Kittel modes and the qubit mediated by a single-cavity mode (see Fig. 1).

(ii) Previous works [22,71,73] only portray the magnon blockade effect of one of the Kittel modes in the strong coupling regime, whereas our proposal more comprehensively investigates the magnon blockade effects of both the Kittel
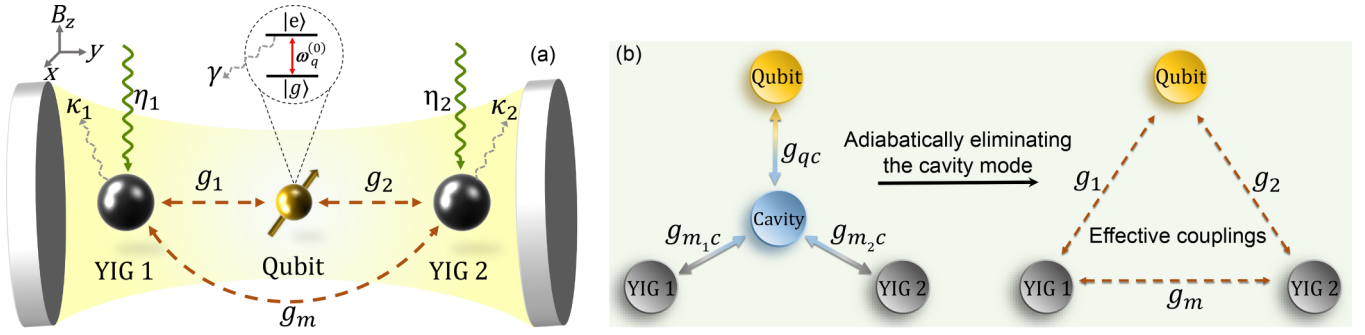
FIG. 1. (a) Schematic diagram of the physical model for the hybrid quantum system which consists of two YIG spheres and one superconducting qubit. The bias magnetic field B_z, which is along the z direction, can be exploited to uniformly magnetize the YIG spheres and adjust the frequencies of the Kittel modes [34]. The x, y, and z axes are defined as shown in the top left corner. Inset (in the dashed circle box): Dirac notations $|e\rangle$ and $|g\rangle$ denote the excited state and the ground state of the two-level qubit, respectively. The red-brown dashed arrows denote the effective couplings, whose strengths are g_1, g_2, and g_m. The green wavy solid arrows represent the drives acting on the Kittel modes, whose strengths are η_1 and η_2. The gray wavy dashed arrows indicate the dissipation of the Kittel modes (κ_1 and κ_2) and the qubit (γ). (b) Schematic diagram of the interactions in the hybrid quantum system. On the left half of this panel, the two-color solid arrows denote the direct couplings between the cavity mode and the two Kittel modes via a magnetic dipole interaction as well as the direct coupling between the cavity mode and the qubit via an electric dipole interaction, whose strengths are g_{m_1c}, g_{m_2c}, and g_{qc}, respectively. Notice that the direct couplings among the two Kittel modes and the qubit are quite weak [6,26,34], so that they can be safely ignored and are not shown in (b). After adiabatically eliminating the cavity mode under the large-detuning condition, the indirect effective couplings can be established among the two Kittel modes and the qubit via the virtual-photon excitation mediated by the cavity mode, which are represented by the red-brown dashed arrows on the right half of this panel and are parametrized by g_1, g_2, and g_m. See text for more details.

modes in the weak qubit-magnon coupling regime, allowing both the Kittel modes to achieve the strong antibunching effects at the same time, i.e., the two-mode magnon blockade effect can be achieved in the microwave band.

(iii) Aside from this, in our proposal we introduce the CSI to constrain the correlations between different Kittel modes, obtaining a maximum CSI violation factor $R = 29.31$ and thus confirming the feasibility of generating quantum correlated magnon pairs with current experimentally accessible parameters.

In the remaining chapters, we organize the article according to the following arrangements. In Sec. II, we describe the physical model of the hybrid YIG quantum system that we consider and gradually provide the total Hamiltonian of this hybrid quantum system, which are the bases of our work. In Sec. III, we analytically calculate the equal-time second-order autocorrelation functions, cross-correlation function, and the CSI by solving the Schrödinger equation. In Sec. IV, we elaborate on the basis and focus of the implementation of our scheme, and set experimentally realistic values for the system parameters. In Sec. V, we introduce the quantum master equation to numerically simulate the equal-time second-order autocorrelation functions, cross-correlation function, and the CSI (Sec. V A). Followed by this, we analyze in detail the modulation of the magnon blockade effects and the quantum correlations by the system parameters (Sec. V B). In Sec. VI, we summarize the main results of our work. Appendixes A–D provide the supplementary details for the derivations which further support our results but are omitted in the main text for readability.

II. PHYSICAL MODEL AND EFFECTIVE HAMILTONIAN

As schematically illustrated in Fig. 1(a), in the considered hybrid ferromagnet-superconductor quantum system,

two YIG spheres and one superconducting qubit are simultaneously placed in a three-dimensional microwave cavity. The two Kittel modes and the qubit are coupled to the same cavity mode through the magnetic dipole and electric dipole interactions, respectively. Direct couplings among the qubit and the two Kittel modes, which are quite weak [6,26,34], can be negligible. Under the condition that the frequencies of the two Kittel modes and the qubit are far from the frequency of the cavity mode, the effective couplings among the qubit and the two Kittel modes can be established via the virtual-photon excitation that is mediated by the cavity mode [33]. A clear and intuitive schematic diagram of these interactions is shown in Fig. 1(b). Such a manipulation is also allowed by the experiments [13,26,29,33]. So we can simplify the calculations by eliminating the cavity mode. The detailed derivation process is provided in Appendix A. In addition, we also verify the reasonableness of such a manipulation by confirming the equivalence between the effective Hamiltonian and the original Hamiltonian in Appendix B. Then we exploit the external driving field to drive the two Kittel modes and express the resulting Hamiltonian of the hybrid system as (presuming $\hbar = 1$ hereafter)

$$\hat{H}_{\text{sys}} = \hat{H}_0 + \hat{H}_{\text{I}} + \hat{H}_{\text{d}}, \tag{1}$$

where

$$\hat{H}_0 = \omega_{m_1}\hat{m}_1^\dagger \hat{m}_1 + \omega_{m_2}\hat{m}_2^\dagger \hat{m}_2 + \omega_q \hat{\sigma}^\dagger \hat{\sigma}, \tag{2a}$$

$$\hat{H}_{\text{I}} = g_1 \hat{m}_1^\dagger \hat{\sigma} + g_2 \hat{m}_2^\dagger \hat{\sigma} + g_m \hat{m}_1^\dagger \hat{m}_2 + \text{H.c.}, \tag{2b}$$

$$\hat{H}_{\text{d}} = \eta_1 \hat{m}_1^\dagger e^{-i\omega_d t} + \eta_2 \hat{m}_2^\dagger e^{-i\omega_d t} + \text{H.c.} \tag{2c}$$

Here, $\hat{H}_0$ denotes the free Hamiltonian of the two Kittel modes and the qubit. $\hat{H}_{\text{I}}$ represents the interaction Hamiltonian among the two Kittel modes and the qubit. $\hat{H}_{\text{d}}$ indicates that the two Kittel modes are pumped by the external driving

field with the same driving frequency ω_d. H.c. denotes the Hermitian conjugate. $\hat{m}_i^\dagger$ ($\hat{m}_i$) ($i = 1, 2$) represents the creation (annihilation) operator of the ith Kittel mode with the effective frequency ω_{m_i}. $\hat{\sigma}^\dagger = |e\rangle\langle g|$ ($\hat{\sigma} = |g\rangle\langle e|$) represents the raising (lowing) operator of the two-level qubit with the effective frequency ω_q. By the virtual-photon excitation mediated by the cavity mode, we can obtain the effective coupling strength $g_i = \frac{1}{2}g_{m_ic}g_{qc}(\frac{1}{\delta_{ic}} + \frac{1}{\delta_{qc}})$ ($i = 1, 2$) [13,29,32] between the ith Kittel mode and the qubit, in which g_{m_ic} (g_{qc}) denotes the direct coupling strength between the ith Kittel mode (the qubit) and the cavity mode, and $\delta_{ic} = \omega_{m_i}^{(0)} - \omega_c$ ($\delta_{qc} = \omega_q^{(0)} - \omega_c$) stands for the frequency detuning between the ith Kittel mode (the qubit) and the cavity mode. $\omega_{m_i}^{(0)}$ ($\omega_q^{(0)}$) represents the bare frequency of the ith Kittel mode (the qubit) and ω_c denotes the frequency of the cavity mode. $g_m = \frac{1}{2}g_{m_1c}g_{m_2c}(\frac{1}{\delta_{1c}} + \frac{1}{\delta_{2c}})$ denotes the effective coupling strength between the two Kittel modes. More details are shown in Appendix A. η_i ($i = 1, 2$) represents the strength of the external driving field acting on the ith Kittel mode. In addition, we also clarify the reason why the long-range effective couplings are introduced via the virtual photon exchange mediated by the cavity mode in Appendix B.

With respect to Appendixes A and C, we would like to emphasize three points: (i) The effective Hamiltonian given by Eq. (1) (see also Appendix A) is accurate in the large-detuning regime where the cavity photon mode is adiabatically eliminated. (ii) The effective Hamiltonian brings insights into the underlying physics about strong indirect qubit-magnon and magnon-magnon couplings that are not normally available from the original Hamiltonian in Appendix C. In particular, the indirect magnon-magnon interplay emerges, which does not exist in the previous works [71,73]. (iii) The effective Hamiltonian allows us to determine analytical solutions of the second-order correlation functions easily as will be discussed later.

It is obvious that the Hamiltonian of the hybrid quantum system above displays explicit time dependence. In order to facilitate the subsequent calculations, we utilize the unitary operator $\hat{U}(t) = e^{-i\omega_d t(\hat{m}_1^\dagger\hat{m}_1 + \hat{m}_2^\dagger\hat{m}_2 + \hat{\sigma}^\dagger\hat{\sigma})}$ to rotate $\hat{H}_{\text{sys}}$ into an interaction picture, thereby removing its dependence on the time. So, the time-independence Hamiltonian $\hat{H}_r$ can be written as

$$\begin{aligned}\hat{H}_r = &\Delta\hat{m}_1^\dagger\hat{m}_1 + (\Delta + \delta_m)\hat{m}_2^\dagger\hat{m}_2 + (\Delta + \delta_q)\hat{\sigma}^\dagger\hat{\sigma} \\ &+ (g_1\hat{m}_1^\dagger\hat{\sigma} + g_2\hat{m}_2^\dagger\hat{\sigma} + g_m\hat{m}_1^\dagger\hat{m}_2 + \text{H.c.}) \\ &+ \eta_1(\hat{m}_1^\dagger + \hat{m}_1) + \eta_2(\hat{m}_2^\dagger + \hat{m}_2),\end{aligned} \quad (3)$$

where $\Delta = \omega_{m_1} - \omega_d$, $\Delta_m = \Delta + \delta_m$, and $\Delta_q = \Delta + \delta_q$ define the frequency detunings between the driving field and the first Kittel mode, the second Kittel mode, and the qubit, respectively. $\delta_m = \omega_{m_2} - \omega_{m_1}$ ($\delta_q = \omega_q - \omega_{m_1}$) represents the

frequency detuning between the second Kittel mode (the qubit) and the first Kittel mode.

Alternatively, by introducing dissipation terms of the hybrid quantum system into $\hat{H}_r$, we can obtain the non-Hermitian Hamiltonian $\hat{H}_{\text{tot}}$, with the form

$$\hat{H}_{\text{tot}} = \hat{H}_r - i\frac{\kappa_1}{2}\hat{m}_1^\dagger\hat{m}_1 - i\frac{\kappa_2}{2}\hat{m}_2^\dagger\hat{m}_2 - i\frac{\gamma}{2}\hat{\sigma}^\dagger\hat{\sigma}, \quad (4)$$

where κ_i (γ) denotes the dissipation of the ith Kittel mode (the two-level qubit). The starting point for Eq. (4) is to gain analytical insight into the problem based on Schrödinger equation for the wave function in Sec. III below. Nevertheless, Eq. (3) is used for our numerical simulations based on quantum master equation for the density matrix in Sec. V.

III. ANALYTICAL CALCULATIONS OF EQUAL-TIME SECOND-ORDER CORRELATION FUNCTIONS AND CSI UNDER WEAK-DRIVING SCENARIO

A. Solving Schrödinger equation analytically under weak-driving scenario

In this section, in order to gain physical insights into the statistical properties of the magnon and the violation of classical CSI, we present the process of approximate analytical calculations for the second-order correlation functions by solving the Schrödinger equation under the condition of the weak-driving limit.

Following the method introduced in Refs. [47,48], only the lower-energy levels of the hybrid quantum system can be excited to the higher-energy levels due to the weak-driving limit. Under such a condition, therefore we can truncate the magnon number state (Fock state) into a few excitation subspace, i.e., the two-magnon excitation subspace, and the wave function can be approximately expanded as

$$\begin{aligned}|\psi\rangle \approx &C_{g00}|g, 0, 0\rangle + C_{g10}|g, 1, 0\rangle + C_{g01}|g, 0, 1\rangle \\ &+ C_{g11}|g, 1, 1\rangle + C_{g20}|g, 2, 0\rangle + C_{g02}|g, 0, 2\rangle \\ &+ C_{e00}|e, 0, 0\rangle + C_{e10}|e, 1, 0\rangle + C_{e01}|e, 0, 1\rangle, \quad (5)\end{aligned}$$

where $|e\rangle$ and $|g\rangle$ correspond to the excited and ground states of the two-level qubit, respectively. $|m_i\rangle$ ($i = 1, 2$) represents the ith Kittel-mode magnon Fock state [29]. When the qubit is in the $|j\rangle$ ($j = g, e$) state and the magnon excitation number of the ith Kittel mode is m_i, the occupying probability of the state $|j, m_1, m_2\rangle$ corresponds to $|C_{jm_1m_2}|^2$ [46].

So far, we have got the total Hamiltonian $\hat{H}_{\text{tot}}$ and the reasonably approximate wave function $|\psi\rangle$ of the hybrid quantum system. Then, by solving the Schrödinger equation $i\frac{\partial|\psi\rangle}{\partial t} = \hat{H}_{\text{tot}}|\psi\rangle$, we can obtain a set of dynamical evolution equations of the probability amplitudes $C_{jm_1m_2}$. The details of solving the Schrödinger equation are provided in Appendix D. The analytical solutions of several important probability amplitudes are yielded as follows:

$$C_{g10} = \frac{[dg_1^2(p - d) - g_m p\Delta' + \Delta'^2]\eta_1}{\Lambda_1}, \quad (6a)$$

$$C_{g01} = \frac{[g_1^2(d - p) - g_m\Delta' + p\Delta'^2]\eta_1}{\Lambda_1}, \quad (6b)$$

$$C_{g11} = \frac{-\left[d^5 g_1^6 + d^3 g_1^4 \chi_1 + d g_1^2 \chi_2 - (g_m p - \Delta')\Delta' \chi_3\right]\eta_1^2}{\Lambda_1 \Lambda_2}, \tag{6c}$$

$$C_{g20} = \frac{\left[d^6 g_1^6 - 2 d^5 g_1^6 p + d^3 g_1^4 \chi_4 + (-g_m p + \Delta')\chi_5 + d^2 g_1^2 \chi_6\right]\eta_1^2}{\sqrt{2}\,\Lambda_1 \Lambda_2}, \tag{6d}$$

$$C_{g02} = \frac{\left[g_1^6 p^2 + 2\Delta'(g_m - p\Delta')\chi_7 - g_1^4 p\left(g_m^2 p - 2 g_m \Delta' + 7 p \Delta'^2\right) + d^3 g_1^4 \chi_8 + d g_1^2 \chi_9\right]\eta_1^2}{\sqrt{2}\,\Lambda_1 \Lambda_2}, \tag{6e}$$

where

$$\chi_1 = -2 g_m^2 + g_1^2 (1 + p^2) + 4 g_m p \Delta' - 2(3 + p^2)\Delta'^2 + d\left[-2 g_1^2 p + \Delta'(p\Delta' - g_m)\right], \tag{7a}$$

$$\chi_2 = g_1^4 p^2 - 2 g_m^3 p \Delta' + 4 g_m^2 (1 + p^2)\Delta'^2 - 22 g_m p \Delta'^3 + 8(1 + p^2)\Delta'^4 - 2 g_1^2 \left(g_m^2 p^2 - 2 g_m p \Delta' + \Delta'^2 + 3 p^2 \Delta'^2\right)$$
$$+ d\left[-2 g_1^4 p + g_1^2 \Delta'(g_m + g_m p^2 + 10 p \Delta') - 2\Delta'(g_m - p\Delta')(g_m^2 - g_m p \Delta' - 3\Delta'^2)\right], \tag{7b}$$

$$\chi_3 = g_1^4 p + 2\Delta'(g_m - p\Delta')(g_m^2 - 4\Delta'^2) + 2 g_1^2 (g_m^2 p - g_m \Delta' - 3 p \Delta'^2), \tag{7c}$$

$$\chi_4 = d\left[-g_m^2 + g_1^2 (1 + p^2) + 2 g_m p \Delta' - 7\Delta'^2\right] - 2 p\left(g_1^2 - g_m^2 + g_m p \Delta' - 6\Delta'^2\right), \tag{7d}$$

$$\chi_5 = (-g_m p + \Delta')\left[g_1^4 - 2(g_1 - g_m)(g_1 + g_m)\Delta'^2 - 8\Delta'^4\right] - 2 d g_1^2 \left[g_1^2 (g_m - 2 p \Delta') + \Delta'(g_m^2 p - 3 g_m \Delta' + 8 p \Delta'^2)\right], \tag{7e}$$

$$\chi_6 = g_1^4 p^2 + 2(g_m p - \Delta')\Delta'\left(2 g_m^2 - g_m p \Delta' - 7\Delta'^2\right) + g_1^2\left[-g_m^2(-1 + p^2) - 2(1 + 2 p^2)\Delta'^2\right], \tag{7f}$$

$$\chi_7 = \Delta'(g_m - p\Delta')\left(g_m^2 - 4\Delta'^2\right) - g_1^2\left(-2 g_m^2 p + g_m \Delta' + 7 p \Delta'^2\right), \tag{7g}$$

$$\chi_8 = -2\left[g_1^2 p - (g_m p - 2\Delta')(g_m - p\Delta')\right] + d\left[g_1^2 + (g_m - p\Delta')^2\right], \tag{7h}$$

$$\chi_9 = -2\left[g_1^4 p + \Delta'(-g_m + p\Delta')\left(g_m^2 - 3 g_m p \Delta' + 8\Delta'^2\right) + g_1^2 (-g_m^2 p + g_m \Delta' - 6 p \Delta'^2)\right]$$
$$+ d\left\{g_1^4 (1 + p^2) - 2\Delta'^2 (g_m - p\Delta')^2 + g_1^2\left[g_m^2(-1 + p^2) - 2(2 + p^2)\Delta'^2\right]\right\}, \tag{7i}$$

$$\Lambda_1 = -2 d g_1^2 g_m + \left[(1 + d^2) g_1^2 + g_m^2\right]\Delta' - \Delta'^3, \tag{7j}$$

$$\Lambda_2 = 2 d g_1^2 g_m\left[g_m^2 - (1 + d^2) g_1^2\right] + \left[(1 + d^2)^2 g_1^4 + 2 g_m^4\right]\Delta' + 10 d g_1^2 g_m \Delta'^2 - \left[6(1 + d^2) g_1^2 + 10 g_m^2\right]\Delta'^3 + 8\Delta'^5. \tag{7k}$$

For the sake of brevity, we further define $d = g_2/g_1$ and $p = \eta_2/\eta_1$ in Eqs. (6) and (7) above.

The other probability amplitudes can also be iteratively calculated, but their contributions to the equal-time second-order correlation functions [i.e., Eqs. (10a)–(10c) in Sec. III B later] can be ignored. Therefore, they are not shown here. As final remark, we point out that the steady-state solutions (6a)–(6e) of the probability amplitudes are the central results in this subsection.

In addition, based on the set of dynamical evolution equations, i.e., Eqs. (D1a)–(D1h) in Appendix D, we can sketch the energy levels and the transition pathways of the hybrid quantum system as indicated in Fig. 2. It is clear that there are multiple transition pathways that can be adopted to reach the two-magnon excitation states. The destructive quantum interference occurs between different excitation pathways, which can suppress the occupation of the two-magnon excitation states, i.e., $|g, 2, 0\rangle$, $|g, 0, 2\rangle$, and $|g, 1, 1\rangle$. In the next subsection, we will make full use of the steady-state solutions of the probability amplitudes to obtain the analytical expressions of the equal-time second-order autocorrelation functions, cross-correlation function, and the CSI of the system, respectively.

B. Normalized equal-time second-order autocorrelation functions $g_{11}^{(2)}(0)$, $g_{22}^{(2)}(0)$ and cross-correlation function $g_{12}^{(2)}(0)$

The common tool used to study the statistical characteristics of the magnons and explore the magnon blockade effect is the second-order correlation function. There are two types of the normalized equal-time second-order correlation functions, i.e., the normalized equal-time second-order autocorrelation function $g_{aa}^{(2)}(0)$ and the normalized equal-time second-order cross-correlation function $g_{ab}^{(2)}(0)$ ($a \neq b$, $a, b = 1, 2$) for both Kittel modes of concern, given by [49]

$$g_{aa}^{(2)}(0) = \frac{\langle \psi_s | \hat{m}_a^{\dagger 2} \hat{m}_a^2 | \psi_s \rangle}{\langle \psi_s | \hat{m}_a^\dagger \hat{m}_a | \psi_s \rangle^2}, \tag{8a}$$

$$g_{ab}^{(2)}(0) = \frac{\langle \psi_s | \hat{m}_a^\dagger \hat{m}_b^\dagger \hat{m}_b \hat{m}_a | \psi_s \rangle}{\langle \psi_s | \hat{m}_a^\dagger \hat{m}_a | \psi_s \rangle \langle \psi_s | \hat{m}_b^\dagger \hat{m}_b | \psi_s \rangle}. \tag{8b}$$

On the one hand, as far as the equal-time second-order autocorrelation function $g_{aa}^{(2)}(0)$ is concerned, by judging whether the value of $g_{aa}^{(2)}(0)$ is less than unity or not, we can identify three different statistical characteristics of the magnons: (i) The first magnon statistics occurs when $g_{aa}^{(2)}(0)$ exceeds unity. In this case, the statistical characteristics of the magnons follow a super-Poissonian distribution, indicating that the behaviors of the magnons exhibit the classical bunching effect. (ii) The second magnon statistics arises when $g_{aa}^{(2)}(0)$ is equal to unity. In this situation, the statistical characteristics of the magnons follow a Poissonian distribution, indicating that the magnon is in a critical state between the classical states and the quantum states, i.e., the coherent state. (iii) The last magnon statistics appears when $g_{aa}^{(2)}(0)$ is less than unity, indicating that the statistical characteristics of the
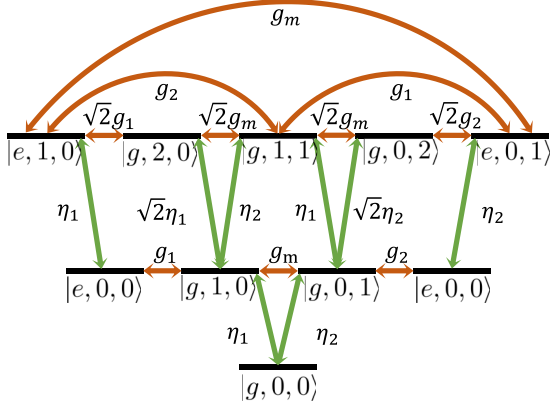
FIG. 2. Schematic representation of the permissible energy levels (horizontal black short lines without arrows) within the truncated subspace and the multiple transition pathways (color lines with arrows). The energy level is represented by $|j, m_1, m_2\rangle$, where j is quantum number in the two-level qubit ($j = e, g$) and m_1, m_2 are the magnon numbers in the two Kittel modes ($m_1, m_2 = 0, 1, 2$). The unconventional magnon blockade originates from the destructive interference between different transition pathways. The effective couplings among the two Kittel modes and the qubit correspond to the red-brown transition pathways, in which an excitation exchange occurs among the two Kittel modes and the qubit. The drives acting on the two Kittel modes correspond to the green transition pathways.

magnons follow sub-Poissonian distribution, and the behaviors of the magnons exhibit the nonclassical antibunching effect. It is worth noting that the values of $g_{aa}^{(2)}(0)$ approaching to zero represent the complete magnon blockade. In this case, the magnons exhibit a tendency to repel or move apart from each other, which can be used to manufacture a single-magnon source.

On the other hand, as far as the equal-time second-order cross-correlation function $g_{ab}^{(2)}(0)$ is concerned, if this condition that $g_{ab}^{(2)}(0)$ is less than unity is satisfied, it indicates that the state $|g, 1, 1\rangle$ is less likely to be occupied. In other words, the excitation of the first Kittel mode will hinder the excitation of the second one, so that the two Kittel modes will not be emitted simultaneously. We can determine that there is an anticorrelation between the two Kittel modes [50,57]. In contrast, if this condition that $g_{ab}^{(2)}(0)$ is larger than unity is satisfied, it represents the excitation of the two-mode magnon pairs. Nevertheless, it is important to emphasize that the value of the equal-time second-order cross-correlation function $g_{ab}^{(2)}(0)$ can not be used straightforwardly to determine that whether the correlations between the two Kittel modes have quantum properties or not, even if it is less than unity. We need to impose a constraint on the equal-time second-order cross-correlation function $g_{ab}^{(2)}(0)$ with other conditions, such as the CSI. Details are presented in Sec. III C later.

In the previous subsection, we have arrived at the probability amplitude of the state $|j, m_1, m_2\rangle$ in the steady state $|\psi_s\rangle$. Analytical expressions for some physical quantities, such as the average magnon occupations of the two Kittel modes, can be approximately expressed by the probability amplitude $C_{jm_1m_2}$. To be specific, under the weak-driving limit, we take the relationship that $C_{g00} \simeq 1 \gg \{C_{g10}, C_{g01}, C_{e00}\} \gg$

$\{C_{g11}, C_{g20}, C_{g02}, C_{e10}, C_{e01}\}$ into consideration, which is also presented by Eq. (D2) in Appendix D. The approximate analytical expressions for the physical quantities associated with the normalized equal-time second-order correlation functions can thus be expressed as

$$\langle\psi_s|\hat{m}_1^{\dagger 2}\hat{m}_1^2|\psi_s\rangle = 2|C_{g20}|^2, \tag{9a}$$

$$\langle\psi_s|\hat{m}_2^{\dagger 2}\hat{m}_2^2|\psi_s\rangle = 2|C_{g02}|^2, \tag{9b}$$

$$\langle\psi_s|\hat{m}_1^\dagger\hat{m}_1|\psi_s\rangle = |C_{g10}|^2 + |C_{g11}|^2 + 2|C_{g20}|^2 + |C_{e10}|^2$$
$$\simeq |C_{g10}|^2, \tag{9c}$$

$$\langle\psi_s|\hat{m}_2^\dagger\hat{m}_2|\psi_s\rangle = |C_{g01}|^2 + |C_{g11}|^2 + 2|C_{g02}|^2 + |C_{e01}|^2$$
$$\simeq |C_{g01}|^2, \tag{9d}$$

$$\langle\psi_s|\hat{m}_1^\dagger\hat{m}_2^\dagger\hat{m}_2\hat{m}_1|\psi_s\rangle = |C_{g11}|^2. \tag{9e}$$

We can substitute the above approximate analytical expressions into the normalized equal-time second-order autocorrelation functions and cross-correlation function [cf. Eqs. (8a) and (8b)], and approximately write them as

$$g_{11}^{(2)}(0) = \frac{\langle\psi_s|\hat{m}_1^{\dagger 2}\hat{m}_1^2|\psi_s\rangle}{\langle\psi_s|\hat{m}_1^\dagger\hat{m}_1|\psi_s\rangle^2} \simeq \frac{2|C_{g20}|^2}{|C_{g10}|^4}, \tag{10a}$$

$$g_{22}^{(2)}(0) = \frac{\langle\psi_s|\hat{m}_2^{\dagger 2}\hat{m}_2^2|\psi_s\rangle}{\langle\psi_s|\hat{m}_2^\dagger\hat{m}_2|\psi_s\rangle^2} \simeq \frac{2|C_{g02}|^2}{|C_{g01}|^4}, \tag{10b}$$

$$g_{12}^{(2)}(0) = \frac{\langle\psi_s|\hat{m}_1^\dagger\hat{m}_2^\dagger\hat{m}_2\hat{m}_1|\psi_s\rangle}{\langle\psi_s|\hat{m}_1^\dagger\hat{m}_1|\psi_s\rangle\langle\psi_s|\hat{m}_2^\dagger\hat{m}_2|\psi_s\rangle}$$
$$\simeq \frac{|C_{g11}|^2}{|C_{g01}|^2|C_{g10}|^2}, \tag{10c}$$

where C_{g10}, C_{g01}, C_{g11}, C_{g20}, and C_{g02} are given by Eqs. (6a)–(6e).

From the above analytical expressions [see, e.g., Eqs. (6a)–(6e) and (7a)–(7k) together with Eqs. (10a)–(10c)], on the one hand, it is easy to find that the items related to the statistical properties of the magnon are sensitively dependent on the controllable parameters of the hybrid system such as the ratio of coupling strengths, the ratio of driving strengths, the driving detunings, and the dissipation, etc. On the other hand, from a mathematical perspective, if we set the probability amplitudes of the two-magnon states equal to zero, i.e., $C_{g20} = 0$, $C_{g02} = 0$, and $C_{g11} = 0$, the normalized equal-time second-order autocorrelation functions $g_{11}^{(2)}(0)$ and $g_{22}^{(2)}(0)$, and cross-correlation functions $g_{12}^{(2)}(0)$ can also be equal to zero, respectively. However, the closed-form conditions of Eqs. (10a)–(10c) in the case of $g_{11}^{(2)}(0) = 0$, $g_{22}^{(2)}(0) = 0$, and $g_{12}^{(2)}(0) = 0$ are too cumbersome to be given here. This will be discussed in more detail in Sec. V B.

In the following, we will associate the equal-time second-order autocorrelation functions $g_{11}^{(2)}(0)$, $g_{22}^{(2)}(0)$ with the equal-time second-order cross-correlation function $g_{12}^{(2)}(0)$ to look into the quantum characteristics of the correlations between the two Kittel modes, such as the violation of classical CSI.

C. Classical CSI and violation of CSI

In this section, we now shift our focus to exploiting the CSI to bound the correlations between the two Kittel

modes [58,59,66,74,75]. To be specific, in our hybrid quantum system, the expectation values of the autocorrelation and cross-correlation magnon numbers follow a relationship which is bounded by the classical CSI [76]:

$$\langle \psi_s | \hat{n}_1 \hat{n}_2 | \psi_s \rangle \leqslant \sqrt{\langle \psi_s | \hat{n}_1^2 | \psi_s \rangle \langle \psi_s | \hat{n}_2^2 | \psi_s \rangle}, \tag{11}$$

where $\hat{n}_i = \hat{m}_i^\dagger \hat{m}_i$ ($i = 1, 2$). It can be easily seen that by adding the same denominator $\langle \psi_s | \hat{n}_1 | \psi_s \rangle \langle \psi_s | \hat{n}_2 | \psi_s \rangle$ to both sides of the above inequality, we can directly achieve the classical CSI expressed with the equal-time second-order autocorrelation functions $g_{11}^{(2)}(0)$, $g_{22}^{(2)}(0)$ and cross-correlation function $g_{12}^{(2)}(0)$ [59,74], namely,

$$g_{12}^{(2)}(0) \leqslant \sqrt{g_{11}^{(2)}(0) g_{22}^{(2)}(0)}. \tag{12}$$

Following Ref. [59], based on Eq. (13), we define a violation factor R and express it as a ratio of $g_{12}^{(2)}(0)$ to $\sqrt{g_{11}^{(2)}(0) g_{22}^{(2)}(0)}$, with the form

$$R = \frac{g_{12}^{(2)}(0)}{\sqrt{g_{11}^{(2)}(0) g_{22}^{(2)}(0)}}, \tag{13}$$

which can describe the degree of the violation for the classical CSI. Specifically, when the value of the violation factor R is less than or equal to unity ($R \leqslant 1$), the correlations between the two Kittel modes follow the classical CSI. However, when the value of the violation factor R is greater than unity ($R > 1$), obviously indicating a violation of the classical CSI (so R called the violation factor), the nonclassical correlations between the two Kittel modes can be well confirmed. Next, we plug Eqs. (10a)–(10c) into the expression of R [38,59], yielding

$$R \simeq \frac{|C_{g11}|^2}{2|C_{g20}||C_{g02}|}, \tag{14}$$

where C_{g11}, C_{g20}, and C_{g02} are yielded by Eqs. (6c)–(6e).

From the expression of the violation factor R, we can make the qualitative conclusions that the values of the violation factor R will be much larger than unity when the moduli of the probability amplitudes for the single-mode two-magnon states (i.e., C_{g20} and C_{g02}) approach to zero. In contrast, the values of the violation factor R will be much less than unity when the modulus of the probability amplitude for the two-mode two-magnon state (i.e., C_{g11}) approaches to zero. In other words, in our hybrid quantum system, the nonclassical correlations between the two Kittel modes exhibit a positive dependence with the degree of the magnon antibunching effect and a negative dependence with the degree of anticorrelation between the two Kittel modes. More detailed descriptions are provided in Sec. V later.

IV. EXPERIMENTAL FEASIBILITY ASSESSMENT AND TYPICAL SYSTEM PARAMETER VALUES

In Sec. II, we describe the physical compositions of our theoretical model as sketched in Fig. 1(a). In this section, we assess the experimental feasibility of the considered hybrid quantum system and determine the typical values of

the relevant system parameters. Based on the available experimental reports in Refs. [1,13,29,33], at a significantly low temperature, we can position a superconducting qubit and two ferromagnetic YIG spheres ($Y_3Fe_5O_{12}$) within a rectangular three-dimensional (3D) microwave cavity [34]. The transmon-type superconducting qubit used in our hybrid quantum system consists of a single Josephson junction ($Al/Al_2O_3/Al$) and two large-area aluminum pads, all of which can be fabricated on a silicon substrate [29]. The 3D microwave cavity can be designed with a combination of oxygen-free copper component and aluminum component [32], the former being smaller in size than the latter [34]. The oxygen-free copper component, which is prepared in a smaller size and exhibits nonsuperconducting property at low temperatures, can enhance the quality factor of the microwave cavity [34]. And the YIG spheres with a diameter of 1 mm should be glued to the oxygen-free copper component [11]. This design facilitates the passage of the applied magnetic field through the oxygen-free copper component for the modulation of the magnon frequencies [32]. The YIG spheres are positioned along the crystal axis $\langle 110 \rangle$, while the static magnetic field B_z which is applied locally to the magnons parallel to the crystal axis $\langle 100 \rangle$, i.e., the z axis [11,26]. This magnetic field is generated by a pair of permanent magnets placed at the ends of a magnetic yoke, which can be tuned by controlling the current in the superconducting coil [11,29]. The aluminum component, to which the qubit is affixed, is additionally enveloped by a pure iron cavity [33,34]. This double-magnetic shielding structure effectively safeguards the qubit against the magnetic field interference and enables it to maintain high coherence [29,34]. In addition, in order to enhance the interaction between the YIG spheres (the qubit) and the cavity mode, it is necessary to place the YIG spheres (the qubit) close to the antinode of the magnetic (electric) field component of the cavity mode [34]. Then the Kittel modes (the qubit) can couple with the magnetic (electric) field component of the cavity mode via a magnetic (an electric) dipole interaction [33], which is characterized by the direct coupling strength $g_{m_{i=1,2}c}$ (g_{qc}).

Based on the aforementioned bases and focus of the experimental implementation platform, we set appropriate values for the system parameters that are permitted by the experiments [13,29,32–34]. We set the dissipation of the first Kittel mode (the qubit) to the value of $\kappa_1/2\pi = 1$ MHz ($\gamma/2\pi = 1$ MHz) with $\kappa_2/\kappa_1 = l$. The coupling strength between the first Kittel mode (the qubit) and the cavity mode, which is in the strong magnon-photon (or qubit-photon) coupling regime in the original cavity-qubit-magnon system, is set to the value of $g_{m_1c}/2\pi = 15$ MHz ($g_{qc}/2\pi = 189$ MHz) with $g_{m_2c}/g_{m_1c} = d$. After the cavity mode is adiabatically eliminated, considering that in the simplified qubit-magnon system our discussions and studies are conducted in the weak qubit-magnon coupling regime, we can take the effective coupling strength between the first Kittel mode and the qubit to be $g_1/2\pi = 0.4$ MHz, which is less than their dissipations. We apply a weak-driving field whose strength is $\eta_1/2\pi = 0.001$ MHz to excite the first Kittel mode with $\eta_2/\eta_1 = p$. Unless otherwise noted, we consistently adopt these typical values of the system parameters.

Finally, we briefly comment on the measurement method of the second-order correlation functions in our scheme. On

the one hand, by coupling the magnon mode to the photon mode and encode the magnon correlations onto the photon correlations, we can exploit a Hanbury Brown–Twiss interferometer [77,78] to measure the second-order correlation functions of the photons, thus indirectly measuring the second-order correlation functions of the magnons [5,79]. Similar methods have also been applied to detect the phonon correlations in optical mechanical systems [39,55] and have been experimentally implemented [80]. On the other hand, the energy of the microwave photons is much lower than that of the optical photons, which makes it difficult to measure individual microwave photon [81], therefore, the second-order correlation functions of the microwave photons cannot be measured by using a usual single-photon detctor. In Ref. [82], an experimental technique based on a linear detector instead of single-photon counters has been proposed and has been successfully developed to measure the second-order correlation functions of the microwave photons in a circuit QED system [81,83]. And magnon is a spin-excited quantum whose frequency is in the range of the microwave bands [84], so we expect that the quantum correlation effects in the magnon-based hybrid quantum systems can be probed by employing the same experimental technique which is described in detail in Ref. [82]. The aforementioned demonstrations indicate the availability of all fundamental components in our architecture.

V. NUMERICAL CALCULATIONS USING MORE PRECISE MASTER-EQUATION APPROACH

A. Dissipative dynamical evolution governed by quantum master equation

In Sec. III, we analytically calculate the normalized equal-time second-order autocorrelation functions $g_{11}^{(2)}(0)$, $g_{22}^{(2)}(0)$, cross-correlation function $g_{12}^{(2)}(0)$, and the violation factor R by solving the Schrödinger equation. In this subsection, we numerically simulate them by employing the full quantum master equation, and demonstrate the consistency between these two methods in the next subsection. With the Born-Markovian approximation, the Lindblad master equation governing the evolution of the system density matrix $\hat{\rho}$ can be written as [85–87]

$$\frac{d\hat{\rho}}{dt} = -i[\hat{H}_r, \hat{\rho}] + \frac{\kappa_1}{2}\hat{\mathcal{L}}[\hat{m}_1]\hat{\rho} + \frac{\kappa_2}{2}\hat{\mathcal{L}}[\hat{m}_2]\hat{\rho} + \frac{\gamma}{2}\hat{\mathcal{L}}[\hat{\sigma}]\hat{\rho},$$

(15)

where $\hat{\mathcal{L}}[\hat{O}]\hat{\rho} = 2\hat{O}\hat{\rho}\hat{O}^\dagger - \hat{O}^\dagger\hat{O}\hat{\rho} - \hat{\rho}\hat{O}^\dagger\hat{O}$ denotes the Lindblad term for the given operator $\hat{O}$ ($\hat{O} = \hat{m}_1$, $\hat{m}_2$, and $\hat{\sigma}$), κ_i ($i = 1, 2$) and γ have been explained previously, and we have assumed zero-temperature environments. When the hybrid quantum system evolves into the steady state $\hat{\rho}_s$, i.e., $\frac{d\hat{\rho}}{dt} = 0$ on the left side of Eq. (16), we can obtain the normalized equal-time second-order autocorrelation functions, cross-correlation function, and the violation factor R which can be expressed as [49]

$$g_{11}^{(2)}(0) = \frac{\mathrm{Tr}(\hat{\rho}_s\hat{m}_1^{\dagger 2}\hat{m}_1^2)}{[\mathrm{Tr}(\hat{\rho}_s\hat{m}_1^\dagger\hat{m}_1)]^2},$$

(16a)

$$g_{22}^{(2)}(0) = \frac{\mathrm{Tr}(\hat{\rho}_s\hat{m}_2^{\dagger 2}\hat{m}_2^2)}{[\mathrm{Tr}(\hat{\rho}_s\hat{m}_2^\dagger\hat{m}_2)]^2},$$

(16b)

$$g_{12}^{(2)}(0) = \frac{\mathrm{Tr}(\hat{\rho}_s\hat{m}_1^\dagger\hat{m}_2^\dagger\hat{m}_2\hat{m}_1)}{\mathrm{Tr}(\hat{\rho}_s\hat{m}_1^\dagger\hat{m}_1)\mathrm{Tr}(\hat{\rho}_s\hat{m}_2^\dagger\hat{m}_2)},$$

(16c)

and

$$R = \frac{\mathrm{Tr}(\hat{\rho}_s\hat{m}_1^\dagger\hat{m}_2^\dagger\hat{m}_2\hat{m}_1)}{\sqrt{\mathrm{Tr}(\hat{\rho}_s\hat{m}_1^{\dagger 2}\hat{m}_1^2)\mathrm{Tr}(\hat{\rho}_s\hat{m}_2^{\dagger 2}\hat{m}_2^2)}},$$

(17)

where Tr means the trace. In what follows, we perform direct numerical simulations of the master equation (16) for our hybrid quantum system. For this purpose, we consider a Hilbert space expanded by the electronic states of the two-level qubit and the magnon Fock states of both Kittel modes. We express the magnon operators on an occupation-number Fock basis, truncated up to 10 magnons to ensure full convergence.

B. Results and discussions about magnon antibunching effect and violation of CSI

In this section, we begin by discussing the dependence of the equal-time second-order autocorrelation functions $g_{11}^{(2)}(0)$ and $g_{22}^{(2)}(0)$, cross-correlation function $g_{12}^{(2)}(0)$, and the violation factor R on the system parameters, such as the ratio of coupling strengths g_{m_2c}/g_{m_1c}, the ratio of driving strengths η_2/η_1, the driving detuning Δ, the frequency detuning δ_m between the two Kittel modes, the frequency detuning δ_q between the first Kittel mode and the qubit, the qubit dissipation γ, and the dissipation ratio κ_2/κ_1 between the two Kittel modes. The detailed results are given in Figs. 3–9.

First of all, in order to explore the independent modulation effect of the ratio of coupling strengths g_{m_2c}/g_{m_1c} and the ratio of driving strengths η_2/η_1 on the magnon blockade effects and the quantum correlations, we consider the same driving detuning $\Delta = \Delta_m = \Delta_q$ (i.e., $\delta_m = \delta_q = 0$) and dissipation $\kappa_1 = \kappa_2 = \gamma$. Based on the above assumption of equal driving detuning, the ratio of effective coupling strengths g_2/g_1 between the two Kittel modes and the qubit is equal to the ratio of coupling strengths g_{m_2c}/g_{m_1c} between the two Kittel modes and the cavity mode. As shown in Fig. 3, the color-scale two-dimensional maps of the equal-time second-order autocorrelation functions $g_{11}^{(2)}(0)$ and $g_{22}^{(2)}(0)$, cross-correlation function $g_{12}^{(2)}(0)$, and the violation factor R are exhibited on a logarithmic scale plotted versus the ratio of coupling strengths g_{m_2c}/g_{m_1c} and the ratio of driving strengths η_2/η_1 simultaneously. The optimal antibunching conditions, anticorrelation conditions, and CSI violation conditions, which can be obtained by setting the analytical solutions C_{g20}, C_{g02}, and C_{g11} in Eqs. (6c)–(6e) to equal to zero, are highlighted in Fig. 3 with the white dashed line, the white dashed-dotted line, and the black dotted lines. These results indicate that the analytical solutions given in Eqs. (10a)–(10c) and (15) are in agreement with the full numerical solutions obtained from the master equation (16). In Fig. 3(c), the region where our hybrid quantum system exhibits a strong anticorrelation is mainly concentrated in the range where g_{m_2c}/g_{m_1c} is less than 1.89. If $g_{11}^{(2)}(0)$, $g_{22}^{(2)}(0)$, and $g_{12}^{(2)}(0)$ are less than unity at the same time, the output of the whole system can be considered as a high-quality single-magnon source. If $g_{11}^{(2)}(0)$ and $g_{22}^{(2)}(0)$ are less than unity while $g_{12}^{(2)}(0)$ is lager than unity, there are no excitation competitions between the two antibunched Kittel
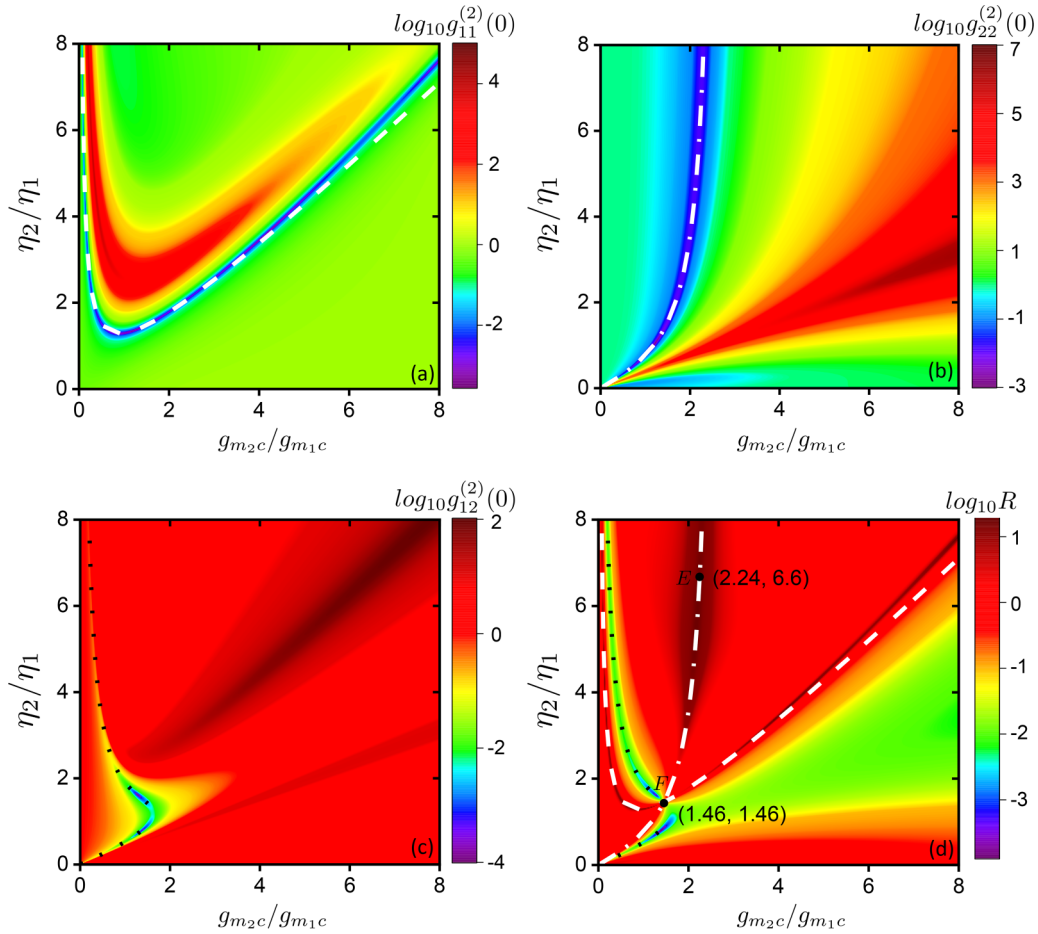
FIG. 3. Logarithmic plot of the equal-time second-order autocorrelation functions $g_{11}^{(2)}(0)$ and $g_{22}^{(2)}(0)$, cross-correlation function $g_{12}^{(2)}(0)$, and the violation factor R versus the ratio of coupling strengths g_{m_2c}/g_{m_1c} and the ratio of driving strengths η_2/η_1 in (a), (b), (c), and (d), respectively. The white dashed and dashed-dotted lines in (a) and (b) represent the analytical solutions given in Eqs. (10a) and (10b) when $g_{11}^{(2)}(0)$ and $g_{22}^{(2)}(0)$ are approximately equal to zero, respectively. The black dotted line in (c) represents the analytical solutions from Eq. (10c) when $g_{12}^{(2)}(0)$ is approximately equal to zero. The white dashed and dashed-dotted lines, and the black dotted line in (d) represent the analytical solutions from Eq. (15) when R reaches its maximal and minimal values, respectively. The point F denotes the intersection of the three lines mentioned in (d) above. The point E denotes a point in the overlap region where the two Kittel modes can achieve magnon antibunching effects simultaneously. The values of the system parameters, taken from Refs. [13,29,32–34], are set as $\Delta = \Delta_m = \Delta_q = 0$, $g_{m_1c}/2\pi = 15$ MHz, $\eta_1/2\pi = 0.001$ MHz, and $\kappa_1/2\pi = \kappa_2/2\pi = \gamma/2\pi = 1$ MHz

modes. Both of these cases are meaningful, so we need to further explore the quantum features, for instance, the violation factor R of the hybrid quantum system with the help of the CSI.

In Fig. 3(d), we show the violation factor R, whose values describe the violation degree of the classical CSI, as a function of the ratio of coupling strengths g_{m_2c}/g_{m_1c} and the ratio of driving strengths η_2/η_1. Comparing with Figs. 3(a), 3(b), and 3(c), we can clearly observe that when the violation factor R reaches its maximal values [corresponding to the white dashed and dashed-dotted lines in Fig. 3(d)], there will be one equal-time second-order autocorrelation function that can reach its minimal values [corresponding to the white dashed and dashed-dotted lines in Figs. 3(a) and 3(d)]. In other words, the optimal CSI violation conditions are the same as the optimal antibunching conditions, which is consistent with the qualitative discussions in Sec. III C. Likewise, when the violation factor R reaches its minimal values [corresponding to the black dotted line in Fig. 3(d)], the equal-time second-order

cross-correlation function $g_{12}^{(2)}(0)$ can also reach its minimal values [corresponding to the black dotted line in Fig. 3(c)]. These results remind us that adjusting the ratio of coupling strengths g_{m_2c}/g_{m_1c} and the ratio of driving strengths η_2/η_1 enable the two Kittel modes to achieve the magnon antibunching effects and generate quantum correlations simultaneously.

To gain a more quantitative insight, here we select the two points of interest [i.e., points E and F in Fig. 3(d)] to further explore the magnon antibunching effects and the quantum correlations. In Fig. 4(a), the equal-time second-order autocorrelation functions $g_{11}^{(2)}(0)$ and $g_{22}^{(2)}(0)$, cross-correlation function $g_{12}^{(2)}(0)$, and the violation factor R are plotted as a function of g_{m_2c}/g_{m_1c} with $\eta_2/\eta_1 = 6.6$ [corresponding to the point E in Fig. 3(d)]. It is obvious that when g_{m_2c}/g_{m_1c} is equal to 2.24, both $g_{11}^{(2)}(0)$ (~ 0.46) and $g_{22}^{(2)}(0)$ ($\sim 2.34 \times 10^{-2}$) are less than unity, whereas both $g_{12}^{(2)}(0)$ (~ 3.05) and R (~ 29.31) are considerably lager than unity, indicating that neither of the single-mode two-magnon states is occupied (i.e., the
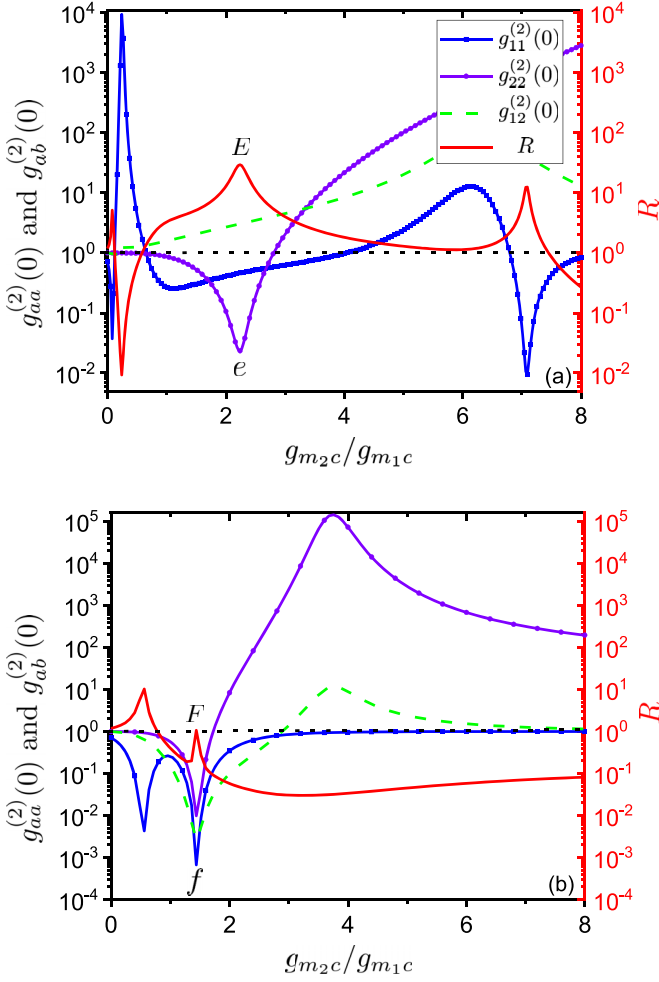
FIG. 4. (a) Dependence of the equal-time second-order auto-correlation functions $g_{11}^{(2)}(0)$ and $g_{22}^{(2)}(0)$, cross-correlation function $g_{12}^{(2)}(0)$, and the violation factor R on the ratio of coupling strengths g_{m_2c}/g_{m_1c} with the ratio of driving strengths $\eta_2/\eta_1 = 6.6$, which describes the situation at the point E in Fig. 3(d). (b) Dependence of the equal-time second-order autocorrelation functions $g_{11}^{(2)}(0)$ and $g_{22}^{(2)}(0)$, cross-correlation function $g_{12}^{(2)}(0)$, and the violation factor R on the ratio of coupling strengths g_{m_2c}/g_{m_1c} with the ratio of driving strengths $\eta_2/\eta_1 = 1.46$, which describes the situation at the point F in Fig. 3(d). The values of the violation factor R described by the red solid lines correspond to the red axis on the right. The black horizontal dotted lines represent the classical threshold for the equal-time second-order autocorrelation functions $g_{11}^{(2)}(0)$ and $g_{22}^{(2)}(0)$, and the violation factor R. The values of the other parameters remain the same as those in Fig. 3.

probability amplitudes of the states $|g, 2, 0\rangle$ and $|g, 0, 2\rangle$ are nearly equal to zero), but the two-mode two-magnon state is occupied (i.e., the probability amplitude of the state $|g, 1, 1\rangle$ is not equal to zero). Therefore, both of the Kittel modes can achieve the magnon antibunching effects, and the correlated magnon pairs highly violate the classical CSI, thus achieving the quantum correlations. In Fig. 4(b), the equal-time second-order autocorrelation functions $g_{11}^{(2)}(0)$ and $g_{22}^{(2)}(0)$, cross-correlation function $g_{12}^{(2)}(0)$, and the violation factor R are plotted as a function of g_{m_2c}/g_{m_1c} with $\eta_2/\eta_1 = 1.46$ [corresponding to the point F in Fig. 3(d)]. The point F is
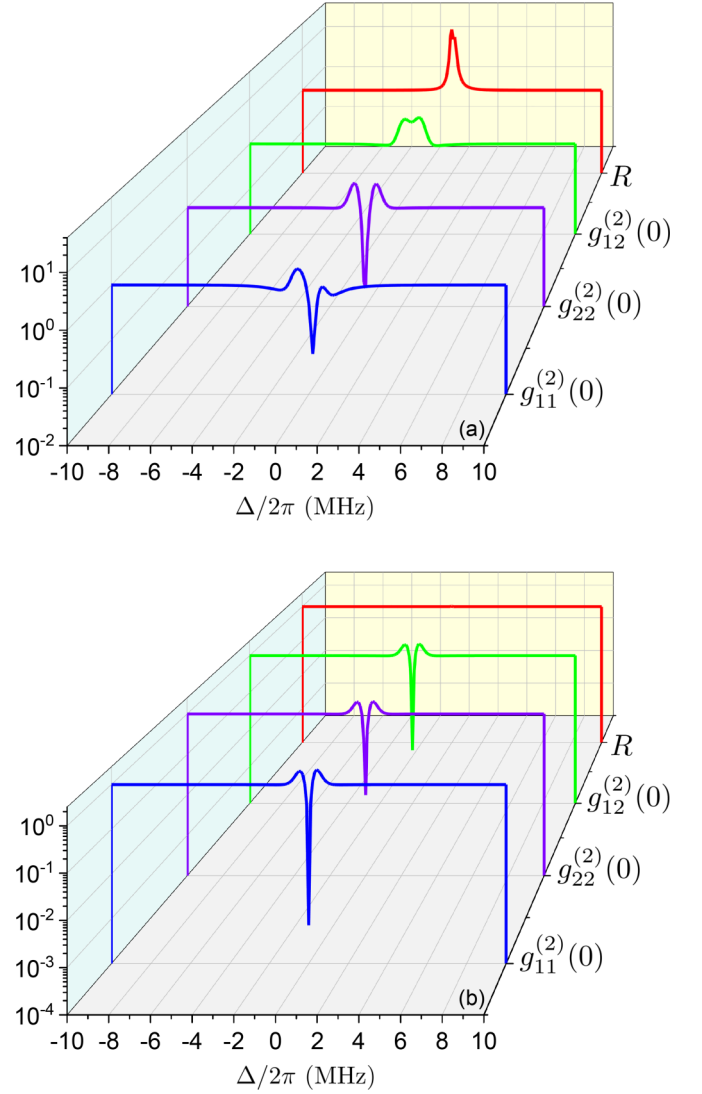

FIG. 5. Dependence of the equal-time second-order autocorrelation functions $g_{11}^{(2)}(0)$ and $g_{22}^{(2)}(0)$, cross-correlation function $g_{12}^{(2)}(0)$, and the violation factor R on the driving detuning Δ with $(g_{m_2c}/g_{m_1c}, \eta_2/\eta_1) = (2.24, 6.6)$ in (a) and $(g_{m_2c}/g_{m_1c}, \eta_2/\eta_1) = (1.46, 1.46)$ in (b). The values of the other parameters remain the same as those in Fig. 3.

the intersection of the white dashed line, the white dashed-dotted line, and the black dotted line. When g_{m_2c}/g_{m_1c} is equal to 1.46, $g_{11}^{(2)}(0)$ ($\sim 7.28 \times 10^{-4}$), $g_{22}^{(2)}(0)$ ($\sim 1.16 \times 10^{-2}$), and $g_{12}^{(2)}(0)$ ($\sim 3.65 \times 10^{-3}$) are less than unity at the same time, while R is approximately equal to unity, suggesting that all of the two-magnon states (including the two-mode two-magnon state) are not occupied. As a consequence, both of the Kittel modes can achieve strong antibunching effects, and there is a strong anticorrelation between them [55]. These results can be utilized to prepare a high-quality single-magnon source. But the value of the violation factor R is equal to unity, which means that at the point F, the correlations between different Kittel modes reach the maximum value of the classical correlation.
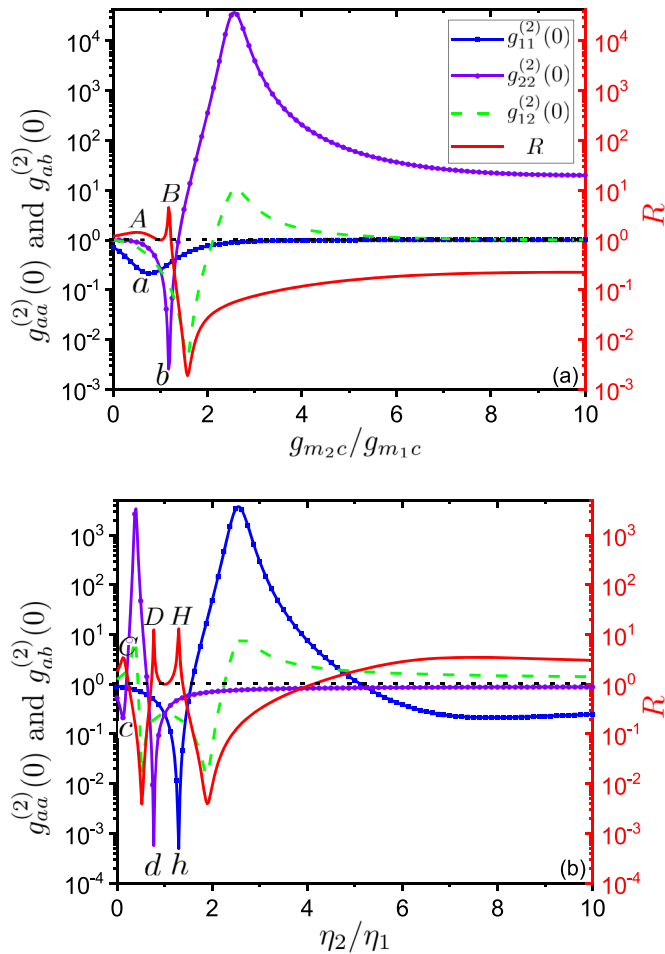
FIG. 6. (a) Dependence of the equal-time second-order auto-correlation functions $g_{11}^{(2)}(0)$ and $g_{22}^{(2)}(0)$, cross-correlation function $g_{12}^{(2)}(0)$, and the violation factor R on the ratio of coupling strengths g_{m_2c}/g_{m_1c} under the conditions of $\eta_2/\eta_1 = 1$ and $g_{m_1c}/2\pi = 15$ MHz. (b) Dependence of the equal-time second-order autocorrelation functions $g_{11}^{(2)}(0)$ and $g_{22}^{(2)}(0)$, cross-correlation function $g_{12}^{(2)}(0)$, and the violation factor R on the ratio of driving strengths η_2/η_1 under the conditions of $g_{m_2c}/g_{m_1c} = 1$ and $\eta_1/2\pi = 0.001$ MHz. The values of the violation factor R described by the red solid lines correspond to the red axis on the right. The uppercase letters (i.e., A, B, C, D, and H) correspond to the maximal values of the violation factor R, and the lowercase letters (i.e., a, b, c, d, and h) correspond to the minimal values of $g_{11}^{(2)}(0)$ or $g_{22}^{(2)}(0)$. The black horizontal dotted lines represent the classical threshold for the equal-time second-order autocorrelation functions $g_{11}^{(2)}(0)$ and $g_{22}^{(2)}(0)$, and the violation factor R. The values of the other parameters remain the same as those in Fig. 3.

In Fig. 5, we additionally demonstrate the influence of the driving detuning on the magnon blockade effects and the quantum correlations between the two Kittel modes under the conditions of the points E and F in Fig. 3(d). It can be observed that the unconventional magnon antibunching effects and the quantum correlations exhibit typical resonance characteristics, which results from the destructive quantum interference. Multiple transition pathways, as shown in Fig. 2, are available for the Kittel modes to choose to reach the two-magnon states. However, by introducing the destructive

quantum interference between different transition pathways, the occupations of the two-magnon states can be prevented, so that the unconventional magnon blockade effect can be achieved.

In order to further investigate the dependence of the equal-time second-order autocorrelation functions $g_{11}^{(2)}(0)$ and $g_{22}^{(2)}(0)$, cross-correlation function $g_{12}^{(2)}(0)$, and the violation factor R on either the ratio of coupling strengths g_{m_2c}/g_{m_1c} or the ratio of driving strengths η_2/η_1, we divide our discussions into the following two cases.

The first case is that we set the ratio of driving strengths to unity, i.e., $p = \eta_2/\eta_1 = 1$. Under this scenario, we look at the independent impact of the ratio of coupling strengths on the modulation of the magnon blockade effects and the quantum correlations between the two Kittel modes. In Fig. 6(a), we plot the equal-time second-order autocorrelation functions $g_{11}^{(2)}(0)$ and $g_{22}^{(2)}(0)$, cross-correlation function $g_{12}^{(2)}(0)$, and the violation factor R as a function of the ratio of coupling strengths g_{m_2c}/g_{m_1c}, under the conditions of $\eta_1/2\pi = \eta_2/2\pi = 0.001$ MHz and $g_{m_1c}/2\pi = 15$ MHz. We primarily focus on the two maximum value points (i.e., points A and B) of the violation factor R. When the ratio of the coupling strengths g_{m_2c}/g_{m_1c} is less than 1.23, the violation factor R remains greater than unity, that is, the correlations between the two Kittel modes are genuinely nonclassical. In addition, when the violation factor R reaches its maximal values (i.e., at the points A and B), one of the equal-time second-order autocorrelation functions can reach its minimal value (i.e., at the points a and b). For example, for the case of positions (A, a), the first Kittel mode can achieve the magnon antibunching effect with $g_{11}^{(2)}(0)$ approximately reaching its minimal value (~ 0.25), while the equal-time second-order autocorrelation function $g_{22}^{(2)}(0)$ of the second Kittel mode is close to unity, indicating that it is in a coherent state. For the case of positions (B, b), the second Kittel mode can achieve the magnon blockade effect with $g_{22}^{(2)}(0)$ reaching its minimal value ($\sim 2.6 \times 10^{-3}$), while the equal-time second-order autocorrelation function $g_{11}^{(2)}(0)$ of the first Kittel mode is close to 0.32. The correlations between the two Kittel modes violate the classical CSI, which implies that under suitable conditions, there are quantum correlations between the two Kittel modes and both of them can realize the magnon antibunching effects. What is noteworthy is that the equal-time second-order cross-correlation function $g_{12}^{(2)}(0)$ is also less than unity, which means that the anticorrelation between the two Kittel modes can be observed. In other words, the excitation of the first Kittel mode hinders the excitation of the second one, that is, there is an excitation competition between the two Kittel modes [88,89].

The second case is that we set the ratio of coupling strengths to unity, i.e., $d = g_{m_2c}/g_{m_1c} = 1$. Under this scenario, we look at the independent impact of the ratio of driving strengths on the modulation of the magnon blockade effects and the quantum correlations between the two Kittel modes. In Fig. 6(b), we plot the equal-time second-order autocorrelation functions $g_{11}^{(2)}(0)$ and $g_{22}^{(2)}(0)$, cross-correlation function $g_{12}^{(2)}(0)$, and the violation factor R as a function of the ratio of driving strengths η_2/η_1, under the conditions of $g_{m_1c}/2\pi = g_{m_2c}/2\pi = 15$ MHz and $\eta_1/2\pi = 0.001$ MHz. In
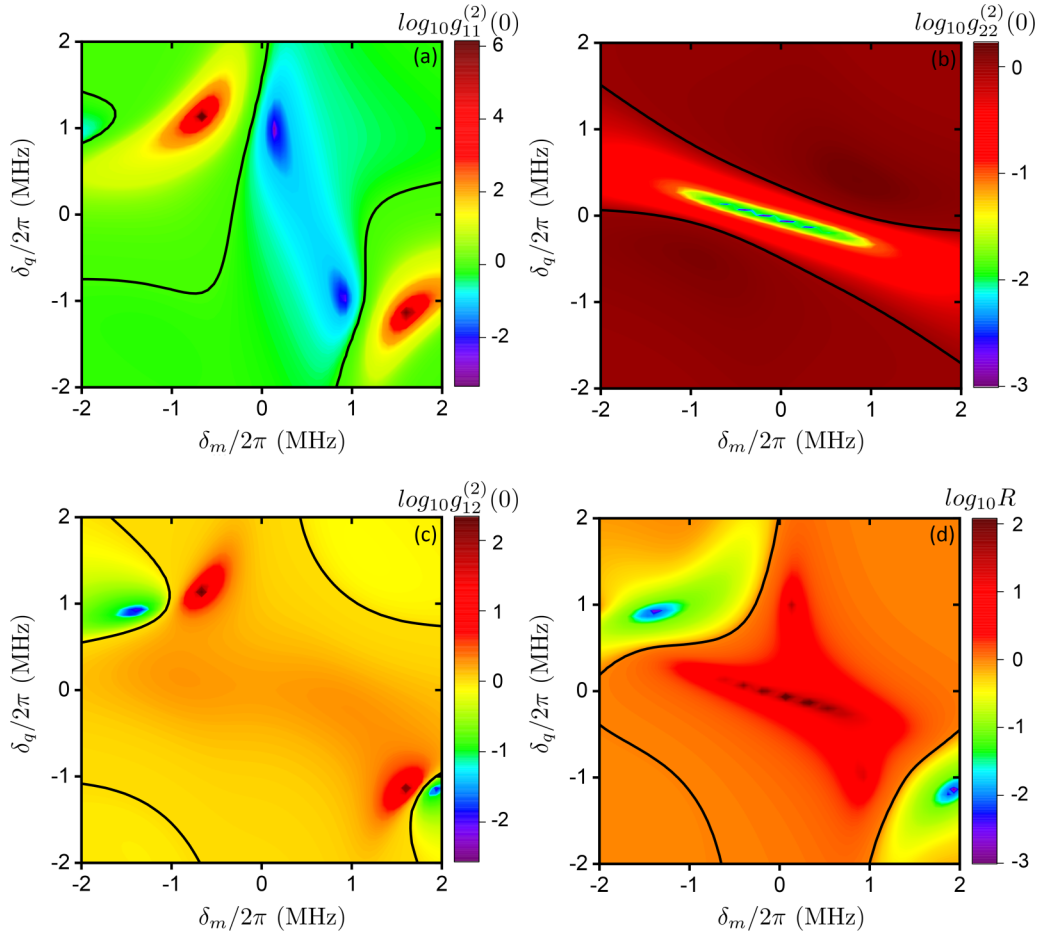
FIG. 7. Logarithmic plot of the equal-time second-order autocorrelation functions $g_{11}^{(2)}(0)$ and $g_{22}^{(2)}(0)$, cross-correlation function $g_{12}^{(2)}(0)$, and the violation factor R versus the frequency detuning δ_m between the two Kittel modes and the frequency detuning δ_q between the first Kittel mode and the qubit in (a), (b), (c), and (d), respectively. The black solid lines in all panels above correspond to $\log_{10} g_{11}^{(2)}(0) = 0$, $\log_{10} g_{22}^{(2)}(0) = 0$, $\log_{10} g_{12}^{(2)}(0) = 0$, and $\log_{10} R = 0$, respectively, which are clear boundaries that separate the classical regime from the pure quantum regime [i.e., $g_{11}^{(2)}(0) < 1$, $g_{22}^{(2)}(0) < 1$, and $R > 1$] [22,90]. The values of the system parameters are set as $\Delta = 0$, $g_{m_2c}/g_{m_1c} = 2.24$, $\eta_2/\eta_1 = 6.6$, and $\kappa_1/2\pi = \kappa_2/2\pi = \gamma/2\pi = 1$ MHz.

this panel, the violation factor R has three maximal values, but not all of them can meet our requirements. When the violation factor R reaches its maximal values (i.e., at the points C, D, and H), the equal-time second-order autocorrelation function of one Kittel mode can reach its minimal value and the equal-time second-order autocorrelation function of the other Kittel mode is also less than unity (i.e., at the points c, d, and h), which is similar to the results of Fig. 6(a). For example, for the case of positions (C, c), the second Kittel mode achieves the magnon antibunching effect $[g_{22}^{(2)}(0) \sim 0.2]$ while the first Kittel mode is close to the coherent state. At the same time, the equal-time second-order cross-correlation function $g_{12}^{(2)}(0)$ also tends to unity. For the cases of positions (D, d) and (H, h), both of the Kittel modes can achieve the magnon antibunching effects, and one of them exhibits a strong antibunching effect. Moreover, we can observe an anticorrelation between the two Kittel modes. When $\eta_2/\eta_1 = 0.775$ (corresponding to the point d), it can be found that $g_{22}^{(2)}(0)$ reaches its minimal value ($\sim 5.93 \times 10^{-4}$), whereas $g_{11}^{(2)}(0)$ does not. Nevertheless, with the increase of η_2/η_1, $g_{11}^{(2)}(0)$ gradually approaches to its minimal value ($\sim 5.34 \times 10^{-4}$) while $g_{22}^{(2)}(0)$ begins to

slowly become larger. The reason for this changing trend is that $g_{12}^{(2)}(0)$ is less than unity, which indicates that there is an excitation competition between the two Kittel modes. In order to realize that both of the Kittel modes can orderly output one by one and the quantum correlations can be established between them, the cases of positions (B, b), (D, d), and (H, h) are undoubtedly better choices. This also means that we have more options by adjusting the ratio of drive strengths rather than the ratio of coupling strengths.

As a side note, the likely reason for this nonmonotonic behavior of the CSI violation parameter R in Figs. 4 and 6 is that the multiple quantum interferences emerge between different excitation pathways from the one-magnon to the two-magnon state (see Fig. 2). However, because of the bulky and tedious expressions of R for the analytical solutions given in Eqs. (6c)–(6e) and (14) where high-order variables are involved, we fail to provide more intuitive physical picture and insight from a quantitative point of view.

In all of the above discussions, we consider $\Delta = \Delta_m = \Delta_q$ (i.e., $\delta_m = \delta_q = 0$), but it is difficult to produce such YIG spheres and qubit which have the same frequency in the manufacturing process. Therefore, it is meaningful to
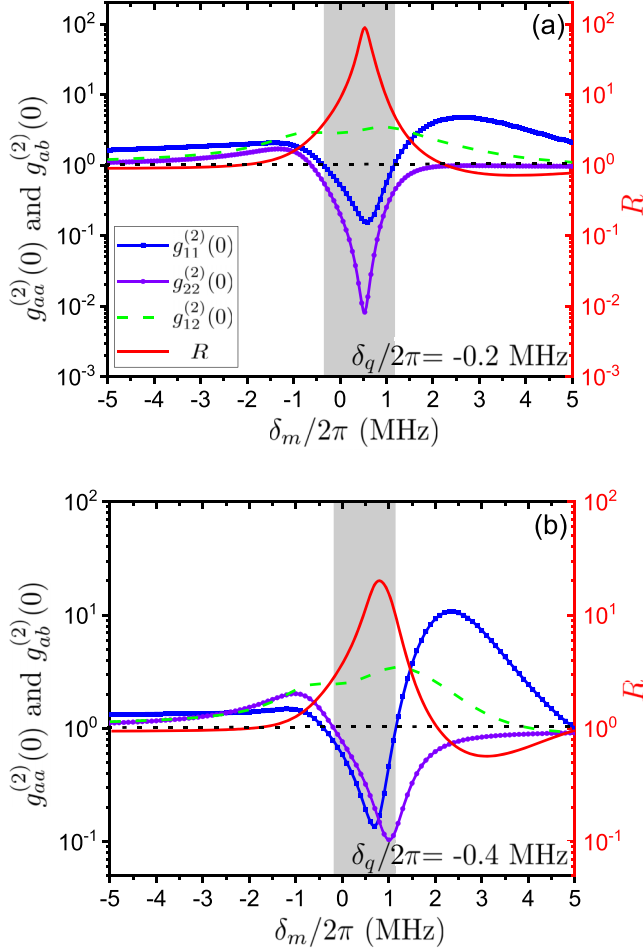
FIG. 8. Dependence of the equal-time second-order autocorrelation functions $g_{11}^{(2)}(0)$ and $g_{22}^{(2)}(0)$, cross-correlation function $g_{12}^{(2)}(0)$, and the violation factor R on the frequency detuning δ_m between the two Kittel modes with $\delta_q/2\pi = -0.2$ MHz in (a) and $\delta_q/2\pi = -0.4$ MHz in (b). The gray shadow areas indicate the region where $g_{11}^{(2)}(0)$ and $g_{22}^{(2)}(0)$ are less than unity simultaneously. The black horizontal dotted lines represent the classical threshold for the equal-time second-order autocorrelation functions $g_{11}^{(2)}(0)$ and $g_{22}^{(2)}(0)$, and the violation factor R. The values of the other parameters remain the same as those in Fig. 7.
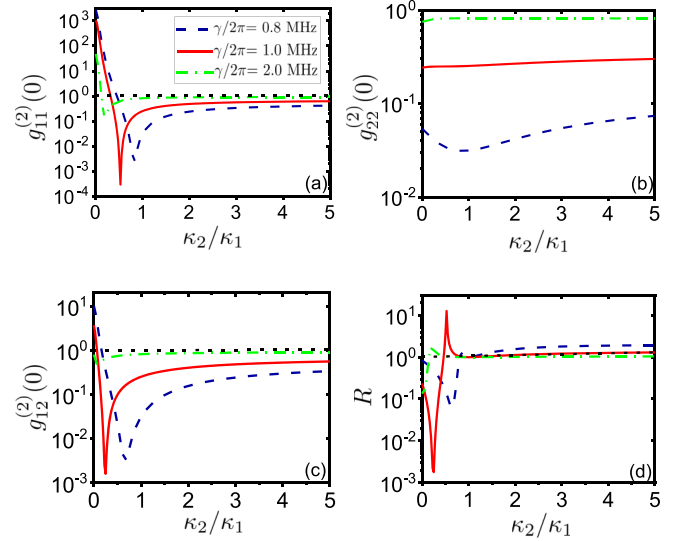

FIG. 9. Dependence of [(a), (b)] the equal-time second-order autocorrelation functions $g_{11}^{(2)}(0)$ and $g_{22}^{(2)}(0)$, [(c)] cross-correlation function $g_{12}^{(2)}(0)$, and [(d)] the violation factor R on the dissipation ratio κ_2/κ_1 between the two Kittel modes with different values of the qubit dissipation γ. The black horizontal dotted lines represent the classical threshold for the equal-time second-order autocorrelation functions $g_{11}^{(2)}(0)$ and $g_{22}^{(2)}(0)$, and the violation factor R. The relevant parameters used here are set as $\Delta = \Delta_m = \Delta_q = 0$, $g_{m_1}/2\pi = g_{m_2}/2\pi = 15$ MHz, $\eta_2/2\pi = \eta_1/2\pi = 0.001$ MHz, and $\kappa_1/2\pi = 1$ MHz.

discuss the influence of the frequency detunings among the two Kittel modes and the qubit on the magnon blockade effects and the quantum correlations. To this end, in Fig. 7, the equal-time second-order autocorrelation functions $g_{11}^{(2)}(0)$ and $g_{22}^{(2)}(0)$, cross-correlation function $g_{12}^{(2)}(0)$, and the violation factor R are plotted on a logarithmic scale as a function of the frequency detuning δ_m between the two Kittel modes and the frequency detuning δ_q between the first Kittel mode and the qubit. As can be seen in Fig. 7(a), the region, in which the first Kittel mode can achieve strong magnon antibunching effect, is concentrated in the range of $\delta_m/2\pi > 0$. In Fig. 7(b), the region, in which the second Kittel mode can achieve strong magnon antibunching effect, is concentrated in the range of -1 MHz $< \delta_m/2\pi < 1$ MHz. And this region is centrosymmetric about the origin. We can clearly observe that there is a region where both $g_{11}^{(2)}(0)$ and $g_{22}^{(2)}(0)$ are less

than unity, indicating that the two Kittel modes can achieve the magnon antibunching effects at the same time by adjusting the frequency detunings among the two Kittel modes and the qubit. In the center of Figs. 7(c) and 7(d), there is a large region, in which both $g_{12}^{(2)}(0)$ and R are greater than unity. In other words, there is an overlapping region where both $g_{11}^{(2)}(0)$ and $g_{22}^{(2)}(0)$ are less than unity, while both $g_{12}^{(2)}(0)$ and R are greater than unity, which means that we can obtain quantum correlated two-mode magnon pairs.

In order to make the description more intuitive, we choose the two specific values in the overlap region to illustrate the aforementioned behaviors. In Fig. 8, we plot the equal-time second-order autocorrelation functions $g_{11}^{(2)}(0)$ and $g_{22}^{(2)}(0)$, cross-correlation function $g_{12}^{(2)}(0)$, and the violation factor R as a function of the frequency detuning δ_m between the two Kittel modes with different frequency detunings δ_q between the first Kittel mode and the qubit. Specifically, in Fig. 8(a), under the condition of $\delta_q/2\pi = -0.2$ MHz, $g_{11}^{(2)}(0)$, $g_{22}^{(2)}(0)$, and R can reach their minimum and maximum values at the same value of $\delta_m/2\pi$, respectively. In addition, there is no excitation competition between the two Kittel modes due to $g_{12}^{(2)}(0) > 1$. In Fig. 8(b), under the condition of $\delta_q/2\pi = -0.4$ MHz, $g_{11}^{(2)}(0)$, $g_{22}^{(2)}(0)$, and R can reach their minimum and maximum values at different values of $\delta_m/2\pi$, respectively. And there is also no excitation competition between the two Kittel modes due to $g_{12}^{(2)}(0) > 1$. In the gray shadow regions marked in Fig. 8, the two Kittel modes can simultaneously realize the magnon antibunching effects, and the two-mode magnon pairs without excitation competition

but with quantum correlations can be achieved. It should be pointed out that the frequency detunings among the two Kittel modes and the qubit (i.e., δ_m and δ_q) need to be as small as possible to achieve the coherent exchange of an efficient magnon excitation in a millimeter-sized ferromagnetic sphere and a superconducting qubit. But this is not contradictory to the large detunings between the cavity mode and the ith Kittel modes (the qubit), i.e., δ_{ic} (δ_{qc}) which can make this cavity mode serve as an intermediary for the exchange of virtual photons among the two Kittel modes and the qubit.

In all the analysis above, we take into account the scenario that $\kappa_1 = \kappa_2 = \gamma$. Next, we focus on how the equal-time second-order autocorrelation functions $g_{11}^{(2)}(0)$ and $g_{22}^{(2)}(0)$, cross-correlation function $g_{12}^{(2)}(0)$, and the violation factor R vary with the dissipation. In Fig. 9, we plot the equal-time second-order autocorrelation functions $g_{11}^{(2)}(0)$ and $g_{22}^{(2)}(0)$, cross-correlation function $g_{12}^{(2)}(0)$, and the violation factor R as a function of the dissipation ratio κ_2/κ_1 between the two Kittel modes under different qubit dissipation γ. In Figs. 9(a) and 9(c), both $g_{11}^{(2)}(0)$ and $g_{12}^{(2)}(0)$ do not vary monotonically with the increase of κ_2/κ_1, so there is always an optimal value of κ_2/κ_1, at which the profiles of $g_{11}^{(2)}(0)$ and $g_{12}^{(2)}(0)$ exhibit a single dip. In Fig. 9(d), the profile of the violation factor R always displays a peak and a dip which correspond to the dips of $g_{11}^{(2)}(0)$ and $g_{12}^{(2)}(0)$, respectively. And when $\gamma/2\pi = 1$ MHz, the degree of the magnon antibunching for the first Kittel mode, anticorrelation between the two Kittel modes, and the violation of the CSI are all at their highest levels. Different from the situations of $g_{11}^{(2)}(0)$, $g_{12}^{(2)}(0)$, and R, in Fig. 9(b), the equal-time second-order autocorrelation function of the second Kittel mode $g_{22}^{(2)}(0)$ is insensitive to the variation of the dissipation ratio κ_2/κ_1. Nevertheless, $g_{22}^{(2)}(0)$ is sensitive to the variation of the qubit dissipation γ. When $\gamma/2\pi$ is 0.8 MHz, the values of $g_{22}^{(2)}(0)$ consistently remain below 0.1, indicating that the second Kittel mode can always achieve the magnon antibunching effect in the range of $0 < \kappa_2/\kappa_1 < 5$. When $\gamma/2\pi$ is 1 MHz, the values of $g_{22}^{(2)}(0)$ are always approximately equal to 0.24. However, when $\gamma/2\pi$ increases to 2 MHz, the values of $g_{22}^{(2)}(0)$ remain around 0.8 which are greater than 0.5. According to these attainable analyses, we can conclude that the equal-time second-order autocorrelation function of the second Kittel mode exhibits robustness against the variation of the dissipation ratio κ_2/κ_1 between the two Kittel modes.

VI. CONCLUSIONS

In summary, we have in detail explored the generation of nonclassical magnon pairs and identified the violation of the CSI in a hybrid ferromagnetic-superconductor quantum system containing two YIG spheres and one superconducting qubit. By the virtual-photon excitation mediated by the same cavity mode, the effective couplings, including the qubit-magnon and magnon-magnon couplings, can be established among the two Kittel modes and the qubit. We acquire the equal-time second-order autocorrelation functions, cross-correlation function, and the degree of the quantum correlations by utilizing two different methods, i.e., analyt-

ical calculations via solving the Schrödinger equation and numerical simulations via solving the full quantum master equation. These methods agree well with each other. Based on the destructive quantum interference between different excitation pathways, we start our research with weak qubit-magnon coupling strengths. The equal-time second-order autocorrelation functions $g_{11}^{(2)}(0)$ and $g_{22}^{(2)}(0)$, cross-correlation function $g_{12}^{(2)}(0)$, and the violation factor R can be modulated by the system parameters, such as the ratio of coupling strengths between the Kittel modes and the cavity mode, the ratio of driving strengths, the driving detuning, the frequency detuning between the Kittel modes, the frequency detuning between the first Kittel mode and the qubit, the qubit dissipation, and the dissipation ratio between the Kittel modes. This reveals the dependence of the magnon statistical properties and the quantum correlations on these system parameters. According to whether the frequencies of the two Kittel modes and the qubit are identical, our research can be classified into the following two cases.

(i) When the frequencies of the two Kittel modes and the qubit are identical, we can control and modulate the magnon statistical properties and the quantum correlations by adjusting the ratio of coupling strengths and the ratio of driving strengths. First of all, there are suitable values for the ratio of coupling strengths and the ratio of driving strengths which allow the two Kittel modes to exhibit antibunching effects simultaneously. Additionally, the correlated magnon pairs violate the CSI, confirming that the correlations between the two Kittel modes are nonclassical. These results offer a scheme to prepare a two-magnon gateway. There are also special values that enable the degrees of both the antibunching effects for the two Kittel modes and the anticorrelation between them to reach their highest levels simultaneously, but the correlations happen not to violate the CSI. These results mean that our proposal offers a feasible route to prepare a high-quality single-magnon source. Furthermore, we investigate the independent modulation effects of either the ratio of coupling strengths or the ratio of driving strengths on the magnon statistical properties and the quantum correlations. We find that by adjusting only one of the two ratios, we enable both of the Kittel modes to achieve the magnon antibunching effects with the excitation competitions and the quantum correlations, which suggests that our hybrid quantum system offers a feasible scheme to prepare a quantum correlated single-magnon source.

(ii) When the frequencies of the two Kittel modes and the qubit are not identical to each other, and the ratio of coupling strengths and the ratio of driving strengths are fixed at suitable values, it is found that we can regulate the magnon statistical properties and the quantum correlations by adjusting the frequency detuning between the two Kittel modes and the frequency detuning between the first Kittel mode and the qubit. In the same parameter regime, the two Kittel modes can exhibit strong antibunching effects simultaneously with the quantum correlations but without excitation competitions. The quantum correlated two-mode magnon pairs can be utilized for preparing the two-magnon gateway. In addition, there are appropriate values for the frequency detunings which enable the degrees of the magnon antibunching effects for the two Kittel modes to reach their highest levels simultaneously.

Last but not least, it is clearly revealed that the statistical properties of the second Kittel mode exhibit robustness against the variation of the dissipation ratio. Our results provide another scheme for achieving the unconventional single-mode or two-mode magnon blockade and obtaining the nonclassically correlated two-mode magnon pairs, which holds potential application value in preparing the high-quality single-magnon sources and the two-magnon gateways in the microwave domain.

ACKNOWLEDGMENTS

APPENDIX A: DERIVATION OF EFFECTIVE COUPLING STRENGTHS AMONG TWO KITTEL MODES AND ONE QUBIT VIA VIRTUAL-PHOTON EXCITATION

In our hybrid ferromagnet-superconductor quantum system [see Fig. 1(a)], there are two Kittel modes and one superconducting qubit, all of which can be coupled to the same cavity mode [see the left half of Fig. 1(b)]. In Eq. (2b), g_i ($i = 1, 2$) and g_m represent the effective coupling strengths. Now, we demonstrate the derivation process of the effective coupling strengths. The original Hamiltonian, which includes the cavity mode, can be divided into two parts:

$$\hat{H}_0^{(0)} = \omega_c \hat{c}^\dagger \hat{c} + \omega_{m_1}^{(0)} \hat{m}_1^\dagger \hat{m}_1 + \omega_{m_2}^{(0)} \hat{m}_2^\dagger \hat{m}_2 + \omega_q^{(0)} \hat{\sigma}^\dagger \hat{\sigma},$$
$$\text{(A1a)}$$

$$\hat{H}_{\mathrm{I}}^{(0)} = g_{m_1c} \hat{m}_1^\dagger \hat{c} + g_{m_2c} \hat{m}_2^\dagger \hat{c} + g_{qc} \hat{\sigma}^\dagger \hat{c} + \text{H.c.,} \quad \text{(A1b)}$$

where ω_c is the frequency of the cavity mode, $\omega_{m_i}^{(0)}$ ($i = 1, 2$) is the bare frequency of the ith Kittel mode, and $\omega_q^{(0)}$ is the bare frequency of the qubit. H.c. stands for the Hermitian conjugate. $\hat{c}^\dagger$ and $\hat{c}$ represent the ladder operators of the cavity mode. $g_{\alpha c}$ means the coupling strength between the cavity mode c and the mode α ($\alpha = m_1, m_2, q$). The other symbols are defined in the text [cf. Eq. (1)].

Below, we can obtain the effective coupling strengths among the two Kittel modes and the qubit by exploiting the Fröhlich-Nakajima transformation [91,92]. To do this, we introduce the unitary operator $\hat{U}' = e^{\hat{S}}$ which satisfies the relation $\hat{H}_{\mathrm{I}}^{(0)} + [\hat{H}_0^{(0)}, \hat{S}] = 0$ [72]. So, after some tedious calculations, the operator $\hat{S}$ can be obtained and written as [93]

$$S = \frac{g_{m_1c}}{\delta_{1c}}(\hat{c}^\dagger \hat{m}_1 - \hat{c} \hat{m}_1^\dagger) + \frac{g_{m_2c}}{\delta_{2c}}(\hat{c}^\dagger \hat{m}_2 - \hat{c} \hat{m}_2^\dagger)$$
$$+ \frac{g_{qc}}{\delta_{qc}}(\hat{c}^\dagger \hat{\sigma} - \hat{c} \hat{\sigma}^\dagger), \quad \text{(A2)}$$

where $\delta_{\alpha c} = \omega_\alpha^{(0)} - \omega_c$ represents the frequency detuning between the mode α and the cavity mode c. The Hamiltonian, which undergoes second-order transformation, can be approximately expressed as

$$\hat{H}^{\mathrm{s}} = \hat{U}'^\dagger (\hat{H}_0^{(0)} + \hat{H}_{\mathrm{I}}^{(0)}) \hat{U}' \approx \hat{H}_0^{(0)} + \frac{1}{2}[\hat{H}_{\mathrm{I}}^{(0)}, \hat{S}]. \quad \text{(A3)}$$

Substituting Eq. (A2) into (A3), we can obtain the Hamiltonian $\hat{H}^{\mathrm{s}}$ containing the terms of effective coupling, which reads as

$$\hat{H}^{\mathrm{s}} = \omega_c \hat{c}^\dagger \hat{c} + \omega_{m_1}^{(0)} \hat{m}_1^\dagger \hat{m}_1 + \omega_{m_2}^{(0)} \hat{m}_2^\dagger \hat{m}_2 + \omega_q^{(0)} \hat{\sigma}^\dagger \hat{\sigma}$$

$$+ \frac{g_{m_1c}^2}{2\delta_{1c}}[2\hat{m}_1^\dagger \hat{m}_1 + 2\hat{c}^\dagger \hat{c}(2\hat{m}_1^\dagger \hat{m}_1 - 1)]$$

$$+ \frac{g_{m_2c}^2}{2\delta_{2c}}[2\hat{m}_2^\dagger \hat{m}_2 + 2\hat{c}^\dagger \hat{c}(2\hat{m}_2^\dagger \hat{m}_2 - 1)]$$

$$+ \frac{g_{qc}^2}{2\delta_{qc}}[2\hat{\sigma}^\dagger \hat{\sigma} + 2\hat{c}^\dagger \hat{c}(2\hat{\sigma}^\dagger \hat{\sigma} - 1)]$$

$$+ \frac{g_{m_1c}g_{qc}}{2}\left(\frac{1}{\delta_{1c}} + \frac{1}{\delta_{qc}}\right)(\hat{m}_1^\dagger \hat{\sigma} + \hat{m}_1 \hat{\sigma}^\dagger)$$

$$+ \frac{g_{m_2c}g_{qc}}{2}\left(\frac{1}{\delta_{2c}} + \frac{1}{\delta_{qc}}\right)(\hat{m}_2^\dagger \hat{\sigma} + \hat{m}_2 \hat{\sigma}^\dagger)$$

$$+ \frac{g_{m_1c}g_{m_2c}}{2}\left(\frac{1}{\delta_{1c}} + \frac{1}{\delta_{2c}}\right)(\hat{m}_1^\dagger \hat{m}_2 + \hat{m}_1 \hat{m}_2^\dagger). \quad \text{(A4)}$$

Here, we emphasize that under the large-detuning limit between the mode α and the cavity mode c, i.e., $|\omega_{m_1}^{(0)} - \omega_c|$, $|\omega_{m_2}^{(0)} - \omega_c|$, and $|\omega_q^{(0)} - \omega_c| \gg g_{m_1c}, g_{m_2c}$, and g_{qc} [33,93], the assumption that the cavity mode c remains in the ground state is reasonable, i.e., $\langle \hat{c}^\dagger \hat{c} \rangle \approx 0$ [72]. For this reason, Eq. (A4) can be further simplified as

$$\hat{H}_{\mathrm{eff}} = \omega_{m_1} \hat{m}_1^\dagger \hat{m}_1 + \omega_{m_2} \hat{m}_2^\dagger \hat{m}_2 + \omega_q \hat{\sigma}^\dagger \hat{\sigma}$$
$$+ g_1(\hat{m}_1^\dagger \hat{\sigma} + \hat{m}_1 \hat{\sigma}^\dagger) + g_2(\hat{m}_2^\dagger \hat{\sigma} + \hat{m}_2 \hat{\sigma}^\dagger)$$
$$+ g_m(\hat{m}_1^\dagger \hat{m}_2 + \hat{m}_1 \hat{m}_2^\dagger), \quad \text{(A5)}$$

where $\omega_{m_1} = \omega_{m_1}^{(0)} + \frac{g_{m_1c}^2}{\delta_{1c}}$, $\omega_{m_2} = \omega_{m_2}^{(0)} + \frac{g_{m_2c}^2}{\delta_{2c}}$, and $\omega_q = \omega_q^{(0)} + \frac{g_{qc}^2}{\delta_{qc}}$ are the corresponding effective frequencies. $g_i = \frac{1}{2}g_{m_ic}g_{qc}(\frac{1}{\delta_{ic}} + \frac{1}{\delta_{qc}})$ ($i = 1, 2$) stands for the effective coupling strength between the ith Kittel mode and the qubit. $g_m = \frac{1}{2}g_{m_1c}g_{m_2c}(\frac{1}{\delta_{1c}} + \frac{1}{\delta_{2c}})$ stands for the effective coupling strength between the two Kittel modes. So far, we successfully eliminate the cavity mode c and establish the effective couplings among the two Kittel modes and the qubit by the virtual-photon excitation mediated by the same cavity mode.

APPENDIX B: PHYSICAL PICTURE OF ESTABLISHING EFFECTIVE COUPLINGS

Although we derive the establishment of the effective couplings in detail in Appendix A, the physical picture of establishing the effective couplings may not be particularly intuitive and clear. In this Appendix, we plan to take the effective coupling between the first Kittel mode and the qubit as an example to address the physical essence of establishing this effective qubit-magnon coupling.

In this case of only considering the first Kittel mode and the qubit in the cavity, the total excitation number operator can be written as $\hat{N} = \hat{\sigma}^\dagger \hat{\sigma} + \hat{m}_1^\dagger \hat{m}_1 + \hat{c}^\dagger \hat{c}$. Below we just consider a single-excitation subspace with $N = 1$ for convenience. That is to say, there exist only three categories of eigenstates, i.e., $|e\rangle_q|0\rangle_{m_1}|0\rangle_c$, $|g\rangle_q|1\rangle_{m_1}|0\rangle_c$, and $|g\rangle_q|0\rangle_{m_1}|1\rangle_c$,
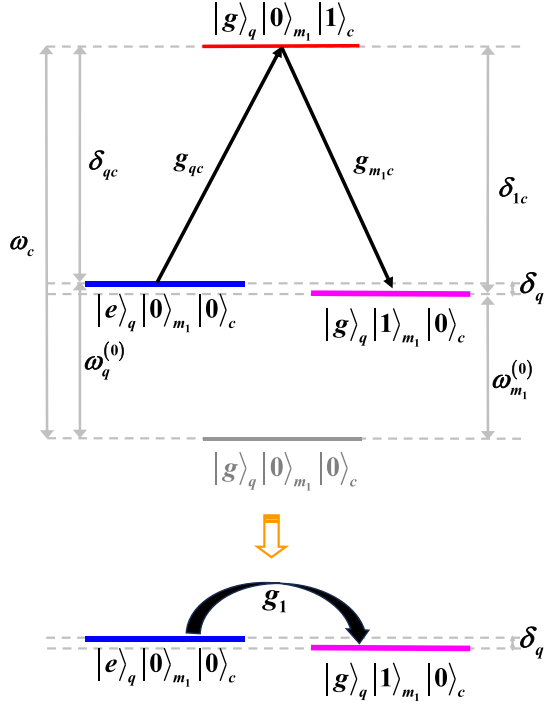
FIG. 10. Energy-level diagram and scheme of establishing the effective qubit-magnon coupling by virtually becoming a photon in the cavity, working in the single-excitation subspace. In the upper panel, the excited state in the qubit $|e\rangle_q|0\rangle_{m_1}|0\rangle_c$ interacts with the excited state in the first Kittel mode $|g\rangle_q|1\rangle_{m_1}|0\rangle_c$ via the exchange of a virtual photon $|g\rangle_q|0\rangle_{m_1}|1\rangle_c$ in the cavity. For convenience, we have taken the energy of the zero-excitation state $|g\rangle_q|0\rangle_{m_1}|0\rangle_c$ to be the zero of energy and $\omega_c > \omega_q^{(0)}, \omega_{m_1}^{(0)}$. Under the large-detuning condition, δ_{qc} and δ_{1c} are much larger than δ_q. The definitions of the relevant parameters in the entire panel are consistent with those in Appendix A.

where the basis vectors $|\cdot\rangle_q$, $|\cdot\rangle_{m_1}$, and $|\cdot\rangle_c$, respectively, stand for the qubit ground or excited state, the Kittel-mode magnon-number state, and the cavity-mode photon-number state. By a concise derivation, we can clarify the reason why the long-range effective qubit-magnon couplings are introduced via the virtual photon exchange mediated by the cavity mode.

Figure 10 clearly shows that, in the single-excitation manifold, an excitation of the two-level qubit from its excited state $|e\rangle_q|0\rangle_{m_1}|0\rangle_c$ can be transferred to the YIG, i.e., a one-magnon state $|g\rangle_q|1\rangle_{m_1}|0\rangle_c$ through a virtual transition via the one-photon intermediate state $|g\rangle_q|0\rangle_{m_1}|1\rangle_c$ in the cavity, and vice versa. That is to say, the excited state of the two-level qubit $|e\rangle_q|0\rangle_{m_1}|0\rangle_c$ interacts with the one-magnon state of the YIG $|g\rangle_q|1\rangle_{m_1}|0\rangle_c$ via the exchange of a virtual photon $|g\rangle_q|0\rangle_{m_1}|1\rangle_c$ in the cavity. In this circumstance, no energy is exchanged with the cavity due to the enough large detuning δ_{1c} (δ_{qc}) between the YIG magnon (the qubit) and the cavity photon, thus revealing that the cavity mode can be adiabatically eliminated. More specifically, in the upper panel of Fig. 10, since the frequencies of the first Kittel mode and the qubit are far from the frequency of the cavity mode, and the frequency of the first Kittel mode is tuned to be nearly resonant with the qubit, virtual photons are created and destroyed and a virtual transition

can be achieved via the intermediate state $|g\rangle_q|0\rangle_{m_1}|1\rangle_c$ [94]. The corresponding transition process depicted in the upper panel of Fig. 10 can be expressed as

$$
\begin{aligned}
\hat{m}_1^\dagger \hat{c} \hat{c}^\dagger \hat{\sigma} |e\rangle_q|0\rangle_{m_1}|0\rangle_c &= (\hat{m}_1^\dagger \hat{c}) \cdot (\hat{c}^\dagger \hat{\sigma}) |e\rangle_q|0\rangle_{m_1}|0\rangle_c \\
&= \hat{m}_1^\dagger \hat{c} |g\rangle_q|0\rangle_{m_1}|1\rangle_c \\
&= |g\rangle_q|1\rangle_{m_1}|0\rangle_c.
\end{aligned} \tag{B1}
$$

From Eq. (B1), it is clear that through the intermediate state $|g\rangle_q|0\rangle_{m_1}|1\rangle_c$, we can achieve the transition from $|e\rangle_q|0\rangle_{m_1}|0\rangle_c$ to $|g\rangle_q|1\rangle_{m_1}|0\rangle_c$. And it is also obvious that $\hat{c}\hat{c}^\dagger|0\rangle_c = |0\rangle_c$ which means that this virtual transition process is mediated by a vacuum field [95]. That is to say, the cavity mode provides a channel as a medium for the exchange of virtual photons between the first Kittel mode and the qubit [96,97].

The lower panel of Fig. 10 describes the interaction between the first Kittel mode and the qubit, which is a transverse interaction of the effective coupling strength g_1. Similarly, the corresponding transition process depicted in the lower panel of Fig. 10 can be represented as

$$
\hat{m}_1^\dagger \hat{\sigma} |e\rangle_q|0\rangle_{m_1}|0\rangle_c = |g\rangle_q|1\rangle_{m_1}|0\rangle_c. \tag{B2}
$$

By comparing Eqs. (B1) and (B2), it is intuitive that the physical picture of the processes depicted in the upper and lower panels of Fig. 10 are consistent, showing that the cavity mode involving the intermediate virtual transition can be adiabatically eliminated. In other words, the qubit-magnon interaction is a result of the virtual exchange of photons via the cavity mode which is far detuned from both the Kittel modes and the qubit. In addition, the effective coupling strength g_1 can be derived by the second-order perturbation theory.

In short, based on Fig. 10 and the concise derivation above, it is straightforward to understand the physical essence of establishing the long-range effective couplings via the virtual photons exchange mediated by the cavity mode.

APPENDIX C: VERIFICATION OF EQUIVALENCE BETWEEN EFFECTIVE HAMILTONIAN AND ORIGINAL HAMILTONIAN

In Appendix A, we present the detailed derivation process of the effective Hamiltonian [i.e., Eq. (A5)], which contains the effective coupling strengths among the two Kittel modes and the qubit. Next, we plan to verify the equivalence between the effective Hamiltonian which has undergone the Fröhlich-Nakajima transformation, and the original Hamiltonian.

To begin with, we apply an external driving field with a frequency of ω_d to the two Kittel modes. On the basis of Eqs. (A1a) and (A1b), we can derive the whole Hamiltonian of the driven hybrid quantum system in Fig. 1(a) as follows:

$$
\hat{H}_{\text{sys}}^{(0)} = \hat{H}_0^{(0)} + \hat{H}_I^{(0)} + \hat{H}_d, \tag{C1}
$$

where $\hat{H}_d = \eta_1 \hat{m}_1^\dagger e^{-i\omega_d t} + \eta_2 \hat{m}_2^\dagger e^{-i\omega_d t} + \text{H.c.}$ denotes the driving Hamiltonian.

Next, we apply the unitary operator $\hat{U}^{(0)}(t) = e^{-i\omega_d t(\hat{c}^\dagger \hat{c} + \hat{m}_1^\dagger \hat{m}_1 + \hat{m}_2^\dagger \hat{m}_2 + \hat{\sigma}^\dagger \hat{\sigma})}$ to transform $\hat{H}_{\text{sys}}^{(0)}$ into a rotating reference frame, thereby eliminating its time dependence. After some calculations, we can rewrite the Hamiltonian of
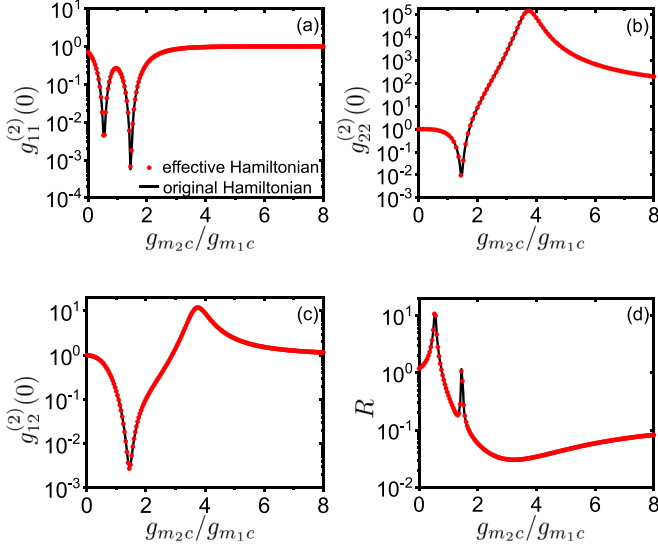
FIG. 11. Comparison of (a), (b) the equal-time second-order autocorrelation functions $g_{11}^{(2)}(0)$ and $g_{22}^{(2)}(0)$, (c) cross-correlation function $g_{12}^{(2)}(0)$, and (d) the violation factor R obtained from the original Hamiltonian (represented by the black solid lines) with those obtained from the effective Hamiltonian (represented by the red dotted lines). The values of the other parameters remain the same as those in Fig. 4(b).

the hybrid quantum system as

$$
\begin{aligned}
\hat{H}_r^{(0)} = {}& \Delta_c^{(0)} \hat{c}^\dagger \hat{c} + \Delta_{m_1}^{(0)} \hat{m}_1^\dagger \hat{m}_1 + \Delta_{m_2}^{(0)} \hat{m}_2^\dagger \hat{m}_2 + \Delta_q^{(0)} \hat{\sigma}^\dagger \hat{\sigma} \\
& + \left(g_{m_1 c} \hat{m}_1^\dagger \hat{c} + g_{m_2 c} \hat{m}_2^\dagger \hat{c} + g_{qc} \hat{\sigma}^\dagger \hat{c} + \text{H.c.} \right) \\
& + \eta_1 (\hat{m}_1^\dagger + \hat{m}_1) + \eta_2 (\hat{m}_2^\dagger + \hat{m}_2), \quad \text{(C2)}
\end{aligned}
$$

where $\Delta_c^{(0)} = \omega_c - \omega_d$ and $\Delta_\alpha^{(0)} = \omega_\alpha^{(0)} - \omega_d$ ($\alpha = m_1, m_2, q$).

Finally, we introduce dissipation terms to obtain a non-Hermitian Hamiltonian $\hat{H}_{tot}^{(0)}$ which does not undergo the Fröhlich-Nakajima transformation, with the form

$$
\begin{aligned}
\hat{H}_{tot}^{(0)} = {}& \hat{H}_r^{(0)} - i\frac{\kappa_c}{2} \hat{c}^\dagger \hat{c} - i\frac{\kappa_1}{2} \hat{m}_1^\dagger \hat{m}_1 - i\frac{\kappa_2}{2} \hat{m}_2^\dagger \hat{m}_2 \\
& - i\frac{\gamma}{2} \hat{\sigma}^\dagger \hat{\sigma}. \quad \text{(C3)}
\end{aligned}
$$

In order to confirm the rationality of the operation in Appendix A, we plan to verify whether the effective Hamiltonian [i.e., Eq. (4)] is equivalent to the original one [i.e., Eq. (C3)]. Using Fig. 4(b) as an example, we additionally plot the equal-time second-order autocorrelation functions $g_{11}^{(2)}(0)$ and $g_{22}^{(2)}(0)$, cross-correlation function $g_{12}^{(2)}(0)$, and the violation factor R under the same conditions with Fig. 4(b), which are completely based on the original Hamiltonian. In Fig. 11, it is evident that the equal-time second-order autocorrelation functions $g_{11}^{(2)}(0)$ and $g_{22}^{(2)}(0)$, cross-correlation function $g_{12}^{(2)}(0)$, and the violation factor R plotted based on the effective Hamiltonian can match well with those plotted based on the original one. Therefore, we can confidently utilize the effective Hamiltonian to solve problems in the hybrid quantum system which we consider.

APPENDIX D: DYNAMICAL EVOLUTION EQUATIONS AND STEADY-STATE SOLUTIONS

In this Appendix, our main aim is to provide the detailed process of solving the Schrödinger equation analytically and to present the formulas that are omitted in the main text. By substituting the non-Hermitian Hamiltonian $\hat{H}_{tot}$ given by Eq. (4) and the wave function $|\psi\rangle$ expressed by Eq. (5) into the Schrödinger equation $i\frac{\partial|\psi\rangle}{\partial t} = \hat{H}_{tot}|\psi\rangle$, we can arrive at the dynamical evolution equations of the probability amplitudes:

$$
\begin{aligned}
i\frac{\partial C_{g10}}{\partial t} = {}& \Delta' C_{g10} + \eta_1 C_{g00} + \eta_2 C_{g11} + \sqrt{2}\eta_1 C_{g20} \\
& + g_1 C_{e00} + g_m C_{g01}, \quad \text{(D1a)}
\end{aligned}
$$

$$
\begin{aligned}
i\frac{\partial C_{g01}}{\partial t} = {}& \Delta_m' C_{g01} + \eta_2 C_{g00} + \eta_1 C_{g11} + \sqrt{2}\eta_2 C_{g02} \\
& + g_2 C_{e00} + g_m C_{g10}, \quad \text{(D1b)}
\end{aligned}
$$

$$
\begin{aligned}
i\frac{\partial C_{g11}}{\partial t} = {}& (\Delta' + \Delta_m') C_{g11} + \eta_2 C_{g10} + \eta_1 C_{g01} + g_2 C_{e10} \\
& + g_1 C_{e01} + \sqrt{2}g_m (C_{g20} + C_{g02}), \quad \text{(D1c)}
\end{aligned}
$$

$$
i\frac{\partial C_{g20}}{\partial t} = 2\Delta' C_{g20} + \sqrt{2}\eta_1 C_{g10} + \sqrt{2}g_1 C_{e10} + \sqrt{2}g_m C_{g11},
$$
$$\text{(D1d)}$$

$$
i\frac{\partial C_{g02}}{\partial t} = 2\Delta_m' C_{g02} + \sqrt{2}\eta_2 C_{g01} + \sqrt{2}g_2 C_{e01} + \sqrt{2}g_m C_{g11},
$$
$$\text{(D1e)}$$

$$
i\frac{\partial C_{e00}}{\partial t} = \Delta_q' C_{e00} + g_1 C_{g10} + g_2 C_{g01} + \eta_1 C_{e10} + \eta_2 C_{e01},
$$
$$\text{(D1f)}$$

$$
\begin{aligned}
i\frac{\partial C_{e10}}{\partial t} = {}& (\Delta' + \Delta_q') C_{e10} + g_2 C_{g11} + \sqrt{2}g_1 C_{g20} \\
& + \eta_1 C_{e00} + g_m C_{e01}, \quad \text{(D1g)}
\end{aligned}
$$

$$
\begin{aligned}
i\frac{\partial C_{e01}}{\partial t} = {}& (\Delta_m' + \Delta_q') C_{e01} + g_1 C_{g11} + \sqrt{2}g_2 C_{g02} \\
& + \eta_2 C_{e00} + g_m C_{e10}, \quad \text{(D1h)}
\end{aligned}
$$

where $\Delta' = \Delta - i\frac{\kappa_1}{2}$, $\Delta_m' = \Delta_m - i\frac{\kappa_2}{2}$, and $\Delta_q' = \Delta_q - i\frac{\gamma}{2}$.

Next, by taking the weak-driving limit, i.e., $\{\eta_1, \eta_2\} \ll \{\kappa_1, \kappa_2, \gamma, g_1, g_2\}$, into consideration, a few energy levels can be excited and most of the magnons and photons stay in the ground state $|g, 0, 0\rangle$. Based on such a condition, we can obtain a relationship as follows:

$$
\begin{aligned}
C_{g00} & \simeq 1 \\
& \gg \{C_{g10}, C_{g01}, C_{e00}\} \\
& \gg \{C_{g11}, C_{g20}, C_{g02}, C_{e10}, C_{e01}\}. \quad \text{(D2)}
\end{aligned}
$$

After this, we can take advantage of the relationship [i.e., Eq. (D2)] above to simplify the dynamical evolution equations and obtain the equations of the probability amplitudes under the steady state $|\psi_s\rangle$, i.e., $i\frac{\partial C_{j m_1 m_2}}{\partial t} = 0$ on the left side of Eqs. (D1a)–(D1h). Concretely, these steady-state probability amplitudes read as

$$
0 = \Delta' C_{g10} + \eta_1 + g_1 C_{e00} + g_m C_{g01}, \quad \text{(D3a)}
$$

$$
0 = \Delta_m' C_{g01} + \eta_2 + g_2 C_{e00} + g_m C_{g10}, \quad \text{(D3b)}
$$

$$0 = (\Delta' + \Delta'_m)C_{g11} + \eta_2 C_{g10} + \eta_1 C_{g01} + g_2 C_{e10}$$
$$+ g_1 C_{e01} + \sqrt{2}g_m C_{g20} + \sqrt{2}g_m C_{g02}, \quad \text{(D3c)}$$

$$0 = 2\Delta'C_{g20} + \sqrt{2}\eta_1 C_{g10} + \sqrt{2}g_1 C_{e10} + \sqrt{2}g_m C_{g11}, \quad \text{(D3d)}$$

$$0 = 2\Delta'_m C_{g02} + \sqrt{2}\eta_2 C_{g01} + \sqrt{2}g_2 C_{e01} + \sqrt{2}g_m C_{g11}, \quad \text{(D3e)}$$

$$0 = \Delta'_q C_{e00} + g_1 C_{g10} + g_2 C_{g01}, \quad \text{(D3f)}$$

$$0 = (\Delta' + \Delta'_q)C_{e10} + g_2 C_{g11} + \sqrt{2}g_1 C_{g20}$$
$$+ \eta_1 C_{e00} + g_m C_{e01}, \quad \text{(D3g)}$$

$$0 = (\Delta'_m + \Delta'_q)C_{e01} + g_1 C_{g11} + \sqrt{2}g_2 C_{g02}$$
$$+ \eta_2 C_{e00} + g_m C_{e10}. \quad \text{(D3h)}$$

It is evident that Eqs. (D3a)–(D3h) are closed, i.e., the number of the unknowns is equal to the number of the equations, allowing us to iteratively calculate the steady-state solutions of all the probability amplitudes. In order to simplify the form of the probability amplitudes, we set $\Delta' = \Delta'_m = \Delta'_q$, $g_2/g_1 = d$, and $\eta_2/\eta_1 = p$, thereby we can attain the probability amplitudes of the single-magnon excitation states (i.e., C_{g10} and C_{g01}) and the two-magnon excitation states (i.e., C_{g20}, C_{g02}, and C_{g11}) given by Eqs. (6a)–(6e) in the main text.

[1] D. Lachance-Quirion, Y. Tabuchi, A. Gloppe, K. Usami, and Y. Nakamura, Hybrid quantum systems based on magnonics, Appl. Phys. Express **12**, 070101 (2019).

[2] B. Z. Rameshti, S. V. Kusminskiy, J. A. Haigh, K. Usami, D. Lachance-Quirion, Y. Nakamura, C.-M. Hu, H. X. Tang, G. E. W. Bauer, and Y. M. Blanter, Cavity magnonics, Phys. Rep. **979**, 1 (2022).

[3] X. Zhang, C.-L. Zou, L. Jiang, and H. X. Tang, Cavity magnomechanics, Sci. Adv. **2**, e1501286 (2016).

[4] A. A. Serga, A. V. Chumak, and B. Hillebrands, YIG magnonics, J. Phys. D: Appl. Phys. **43**, 264002 (2010).

[5] H. Y. Yuan, Y. Cao, A. Kamra, R. A. Duine, and P. Yan, Quantum magnonics: When magnon spintronics meets quantum information science, Phys. Rep. **965**, 1 (2022).

[6] W. Xiong, M. Tian, G.-Q. Zhang, and J. Q. You, Strong long-range spin-spin coupling via a Kerr magnon interface, Phys. Rev. B **105**, 245310 (2022).

[7] T. Neuman, D. S. Wang, and P. Narang, Nanomagnonic cavities for strong spin-magnon coupling and magnon-mediated spin-spin interactions, Phys. Rev. Lett. **125**, 247702 (2020).

[8] X. Zhang, C.-L. Zou, L. Jiang, and H. X. Tang, Strongly coupled magnons and cavity microwave photons, Phys. Rev. Lett. **113**, 156401 (2014).

[9] Y. Cao, P. Yan, H. Huebl, S. T. B. Goennenwein, and G. E. W. Bauer, Exchange magnon-polaritons in microwave cavities, Phys. Rev. B **91**, 094423 (2015).

[10] A. E. Clark and R. E. Strakna, Elastic constants of single-crystal YIG, J. Appl. Phys. **32**, 1172 (1961).

[11] Y. Tabuchi, S. Ishino, T. Ishikawa, R. Yamazaki, K. Usami, and Y. Nakamura, Hybridizing ferromagnetic magnons and microwave photons in the quantum limit, Phys. Rev. Lett. **113**, 083603 (2014).

[12] D. Zhang, X.-M. Wang, T.-F. Li, X.-Q. Luo, W. Wu, F. Nori, and J. Q. You, Cavity quantum electrodynamics with ferromagnetic magnons in a small yttrium-iron-garnet sphere, npj Quantum Inf. **1**, 15014 (2015).

[13] D. Lachance-Quirion, Y. Tabuchi, S. Ishino, A. Noguchi, T. Ishikawa, R. Yamazaki, and Y. Nakamura, Resolving quanta of collective spin excitations in a millimeter-sized ferromagnet, Sci. Adv. **3**, e1603150 (2017).

[14] Z.-B. Yang, J.-S. Liu, H. Jin, Q.-H. Zhu, A.-D. Zhu, H.-Y. Liu, Y. Ming, and R.-C. Yang, Entanglement enhanced by Kerr nonlinearity in a cavity-optomagnonics system, Opt. Express **28**, 31862 (2020).

[15] J. Li, S.-Y. Zhu, and G. S. Agarwal, Squeezed states of magnons and phonons in cavity magnomechanics, Phys. Rev. A **99**, 021801(R) (2019).

[16] C. Kong, B. Wang, Z.-X. Liu, H. Xiong, and Y. Wu, Magnetically controllable slow light based on magnetostrictive forces, Opt. Express **27**, 5544 (2019).

[17] J. Li, S.-Y. Zhu, and G. S. Agarwal, Magnon-photon-phonon entanglement in cavity magnomechanics, Phys. Rev. Lett. **121**, 203601 (2018).

[18] R. Hisatomi, A. Osada, Y. Tabuchi, T. Ishikawa, A. Noguchi, R. Yamazaki, K. Usami, and Y. Nakamura, Bidirectional conversion between microwave and light via ferromagnetic magnons, Phys. Rev. B **93**, 174427 (2016).

[19] S. Viola Kusminskiy, H. X. Tang, and F. Marquardt, Coupled spin-light dynamics in cavity optomagnonics, Phys. Rev. A **94**, 033821 (2016).

[20] Y. Xiao, X. H. Yan, Y. Zhang, V. L. Grigoryan, C. M. Hu, H. Guo, and K. Xia, Magnon dark mode of an antiferromagnetic insulator in a microwave cavity, Phys. Rev. B **99**, 094407 (2019).

[21] X. Zhang, C.-L. Zou, N. Zhu, F. Marquardt, L. Jiang, and H. X. Tang, Magnon dark modes and gradient memory, Nat. Commun. **6**, 8914 (2015).

[22] Z.-X. Liu, H. Xiong, and Y. Wu, Magnon blockade in a hybrid ferromagnet-superconductor quantum system, Phys. Rev. B **100**, 134421 (2019).

[23] X. Li, X. Wang, Z. Wu, W.-X. Yang, and A. Chen, Tunable magnon antibunching in a hybrid ferromagnet-superconductor system with two qubits, Phys. Rev. B **104**, 224434 (2021).

[24] L. Wang, Z.-X. Yang, Y.-M. Liu, C.-H. Bai, D.-Y. Wang, S. Zhang, and H.-F. Wang, Magnon blockade in a $\mathcal{PT}$-symmetric-like cavity magnomechanical system, Ann. Phys. **532**, 2000028 (2020).

[25] Y. Xu, T. Yang, L. Lin, and J. Song, Conventional and unconventional magnon blockades in a qubit-magnon hybrid quantum system, J. Opt. Soc. Am. B **38**, 876 (2021).

[26] Y. Tabuchi, S. Ishino, A. Noguchi, T. Ishikawa, R. Yamazaki, K. Usami, and Y. Nakamura, Quantum Magnonics: The magnon meets the superconducting qubit, C. R. Phys. **17**, 729 (2016).

[27] L. R. Walker, Magnetostatic modes in ferromagnetic resonance, Phys. Rev. **105**, 390 (1957).

[28] L. R. Walker, Resonant modes of ferromagnetic spheroids, J. Appl. Phys. **29**, 318 (1958).

[29] Y. Tabuchi, S. Ishino, A. Noguchi, T. Ishikawa, R. Yamazaki, K. Usami, and Y. Nakamura, Coherent coupling between a ferromagnetic magnon and a superconducting qubit, Science **349**, 405 (2015).

[30] M. H. Devoret and R. J. Schoelkopf, Superconducting circuits for quantum information: An outlook, Science **339**, 1169 (2013).

[31] J. Q. You and F. Nori, Atomic physics and quantum optics using superconducting circuits, Nature (London) **474**, 589 (2011).

[32] Y.-P. Wang, G.-Q. Zhang, D. Xu, T.-F. Li, S.-Y. Zhu, J.-S. Tsai, and J.-Q. You, Quantum simulation of the fermion-boson composite quasi-particles with a driven qubit-magnon hybrid quantum system, arXiv:1903.12498.

[33] D. Lachance-Quirion, S. P. Wolski, Y. Tabuchi, S. Kono, K. Usami, and Y. Nakamura, Entanglement-based single-shot detection of a single magnon with a superconducting qubit, Science **367**, 425 (2020).

[34] D. Xu, X.-K. Gu, H.-K. Li, Y.-C. Weng, Y.-P. Wang, J. Li, H. Wang, S.-Y. Zhu, and J. Q. You, Quantum control of a single magnon in a macroscopic spin system, Phys. Rev. Lett. **130**, 193603 (2023).

[35] R. Huang, A. Miranowicz, J.-Q. Liao, F. Nori, and H. Jing, Nonreciprocal photon blockade, Phys. Rev. Lett. **121**, 153601 (2018).

[36] C. Vaneph, A. Morvan, G. Aiello, M. Féchant, M. Aprili, J. Gabelli, and J. Estève, Observation of the unconventional photon blockade in the microwave domain, Phys. Rev. Lett. **121**, 043602 (2018).

[37] E. Zubizarreta Casalengua, J. C. López Carreño, F. P. Laussy, and E. del Valle, Conventional and unconventional photon statistics, Laser Photon. Rev. **14**, 1900279 (2020).

[38] Z. Peng and Y. Deng, Nonclassical correlated deterministic single-photon pairs for a trapped atom in bimodal cavities, Phys. Rev. A **105**, 043711 (2022).

[39] X.-W. Xu, A.-X. Chen, and Y. Liu, Phonon blockade in a nanomechanical resonator resonantly coupled to a qubit, Phys. Rev. A **94**, 063853 (2016).

[40] H. Xie, C.-G. Liao, X. Shang, Z.-H. Chen, and X.-M. Lin, Optically induced phonon blockade in an optomechanical system with second-order nonlinearity, Phys. Rev. A **98**, 023819 (2018).

[41] N. Didier, S. Pugnetti, Y. M. Blanter, and R. Fazio, Detecting phonon blockade with photons, Phys. Rev. B **84**, 054503 (2011).

[42] J. Xie, S. Ma, and F. Li, Quantum-interference-enhanced magnon blockade in an yttrium-iron-garnet sphere coupled to superconducting circuits, Phys. Rev. A **101**, 042331 (2020).

[43] Y. H. Zhou, X. Y. Zhang, Q. C. Wu, B. L. Ye, Z.-Q. Zhang, D. D. Zou, H. Z. Shen, and C.-P. Yang, Conventional photon blockade with a three-wave mixing, Phys. Rev. A **102**, 033713 (2020).

[44] F. Wang, C. Gou, J. Xu, and C. Gong, Hybrid magnon-atom entanglement and magnon blockade via quantum interference, Phys. Rev. A **106**, 013705 (2022).

[45] C. Zhao, X. Li, S. Chao, R. Peng, C. Li, and L. Zhou, Simultaneous blockade of a photon, phonon, and magnon induced by a two-level atom, Phys. Rev. A **101**, 063838 (2020).

[46] K. Wu, W. Zhong, G. Cheng, and A. Chen, Phase-controlled multimagnon blockade and magnon-induced tunneling in a hybrid superconducting system, Phys. Rev. A **103**, 052411 (2021).

[47] H. Flayac and V. Savona, Unconventional photon blockade, Phys. Rev. A **96**, 053810 (2017).

[48] M. Bamba, A. Imamoğlu, I. Carusotto, and C. Ciuti, Origin of strong photon antibunching in weakly nonlinear photonic molecules, Phys. Rev. A **83**, 021802(R) (2011).

[49] R. Loudon, *The Quantum Theory of Light* (Oxford University Press, Oxford, 2003).

[50] X. Y. Zhang, Y. H. Zhou, Y. Q. Guo, and X. X. Yi, Anticorrelated phonons with two-mode Gaussian squeezed state, Phys. Scr. **95**, 025102 (2020).

[51] L. Li and L. Liu, Phonon blockade and strong anti-correlation between phonons and phonons in the optomechanical system with an auxiliary mechanical oscillator, J. Phys. B: At., Mol. Opt. Phys. **54**, 055401 (2021).

[52] H. Kim, J. Park, H.-G. Hong, T. Y. Kwon, J. Park, and H. S. Moon, Photon-pair generation from a chip-scale Cs atomic vapor cell, Opt. Express **30**, 23868 (2022).

[53] S. Gasparinetti, M. Pechal, J.-C. Besse, M. Mondal, C. Eichler, and A. Wallraff, Correlations and entanglement of microwave photons emitted in a cascade decay, Phys. Rev. Lett. **119**, 140504 (2017).

[54] S. Carlig and M. A. Macovei, Quantum correlations among optical and vibrational quanta, Phys. Rev. A **89**, 053803 (2014).

[55] X.-W. Xu, H.-Q. Shi, A.-X. Chen, and Y. Liu, Cross-correlation between photons and phonons in quadratically coupled optomechanical systems, Phys. Rev. A **98**, 013821 (2018).

[56] R. Riedinger, S. Hong, R. A. Norte, J. A. Slater, J. Shang, A. G. Krause, V. Anant, M. Aspelmeyer, and S. Gröblacher, Non-classical correlations between single photons and phonons from a mechanical oscillator, Nature (London) **530**, 313 (2016).

[57] M. S. Kheirabady and M. K. Tavassoly, Steady state quantum statistics of a hybrid optomechanical-ferromagnet system: photon and magnon blockade, J. Phys. B: At., Mol. Opt. Phys. **56**, 035501 (2023).

[58] M. D. Reid and D. F. Walls, Violations of classical inequalities in quantum optics, Phys. Rev. A **34**, 1260 (1986).

[59] C. Sánchez Muñoz, E. del Valle, C. Tejedor, and F. P. Laussy, Violation of classical inequalities by photon frequency filtering, Phys. Rev. A **90**, 052111 (2014).

[60] C. Laplane, P. Jobez, J. Etesse, N. Gisin, and M. Afzelius, Multimode and long-lived quantum correlations between photons and spins in a crystal, Phys. Rev. Lett. **118**, 210501 (2017).

[61] C. A. Downing, J. C. L. Carreño, A. I. Fernández-Domínguez, and E. del Valle, Asymmetric coupling between two quantum emitters, Phys. Rev. A **102**, 013723 (2020).

[62] K. V. Kheruntsyan, J.-C. Jaskula, P. Deuar, M. Bonneau, G. B. Partridge, J. Ruaudel, R. Lopes, D. Boiron, and C. I. Westbrook, Violation of the Cauchy-Schwarz inequality with matter waves, Phys. Rev. Lett. **108**, 260401 (2012).

[63] Y. Li, P. J. Edwards, X. Huang, and Y. Wang, Violation of a classical Cauchy-Schwarz inequality in photon noise spectra, J. Opt. B: Quantum Semiclass. Opt. **2**, 292 (2000).

[64] J. F. Clauser, Experimental distinction between the quantum and classical field-theoretic predictions for the photoelectric effect, Phys. Rev. D **9**, 853 (1974).

[65] A. Kuzmich, W. P. Bowen, A. D. Boozer, A. Boca, C. W. Chou, L.-M. Duan, and H. J. Kimble, Generation of nonclassical

photon pairs for scalable quantum communication with atomic ensembles, Nature (London) **423**, 731 (2003).

[66] M. Kozierowski, Violation of the Cauchy-Schwarz inequality and anticorrelation effect in second-harmonic generation, Phys. Rev. A **36**, 2973 (1987).

[67] Y. Ren, X. Wang, Y. Lou, S. Liu, Y. Zhong, and J. Jing, Violation of high-dimensional Bell inequality using narrowband orbital-angular-momentum entanglement from warm atomic vapor, Phys. Rev. A **105**, 013721 (2022).

[68] P. Kolchin, S. Du, C. Belthangady, G. Y. Yin, and S. E. Harris, Generation of narrow-bandwidth paired photons: Use of a single driving laser, Phys. Rev. Lett. **97**, 113602 (2006).

[69] M. O. Araújo, L. S. Marinho, and D. Felinto, Observation of nonclassical correlations in biphotons generated from an ensemble of pure two-level atoms, Phys. Rev. Lett. **128**, 083601 (2022).

[70] T. Wasak, P. Szańkowski, P. Ziń, M. Trippenbach, and J. Chwedeńczuk, Cauchy-Schwarz inequality and particle entanglement, Phys. Rev. A **90**, 033616 (2014).

[71] X. Li, G.-L. Cheng, and W.-X. Yang, Tunable magnon antibunching via degenerate three-wave mixing in a hybrid ferromagnet-superconductor system, Appl. Phys. Lett. **121**, 122403 (2022).

[72] Y. Wang, W. Xiong, Z. Xu, G.-Q. Zhang, and J.-Q. You, Dissipation-induced nonreciprocal magnon blockade in a magnon-based hybrid system, Sci. China Phys. Mech. Astron. **65**, 260314 (2022).

[73] P. K. Gupta, S. Kalita, and A. K. Sarma, Quantum interference induced magnon blockade and antibunching in a hybrid quantum system, arXiv:2305.08444.

[74] A. M. Marino, V. Boyer, and P. D. Lett, Violation of the Cauchy-Schwarz inequality in the macroscopic regime, Phys. Rev. Lett. **100**, 233601 (2008).

[75] J. Leppäkangas, G. Johansson, M. Marthaler, and M. Fogelström, Nonclassical photon pair production in a voltage-biased josephson junction, Phys. Rev. Lett. **110**, 267004 (2013).

[76] P. Steindl, H. Snijders, G. Westra, E. Hissink, K. Iakovlev, S. Polla, J. A. Frey, J. Norman, A. C. Gossard, J. E. Bowers, D. Bouwmeester, and W. Löffler, Artificial coherent states of light by multiphoton interference in a single-photon stream, Phys. Rev. Lett. **126**, 143601 (2021).

[77] R. Hanbury Brown and R. Twiss, A test of a new type of stellar interferometer on sirius, Nature (London) **178**, 1046 (1956).

[78] L. De Santis, C. Antón, B. Reznychenko, N. Somaschi, G. Coppola, J. Senellart, C. Gómez, A. Lemaître, I. Sagnes, A. G. White, L. Lanco, A. Auffèves, and P. Senellart, A solid-state single-photon filter, Nat. Nanotechnol. **12**, 663 (2017).

[79] H. Y. Yuan and R. A. Duine, Magnon antibunching in a nanomagnet, Phys. Rev. B **102**, 100402(R) (2020).

[80] J. D. Cohen, S. M. Meenehan, G. S. MacCabe, S. Groblacher, A. H. Safavi-Naeini, F. Marsili, M. D. Shaw, and O. Painter, Phonon counting and intensity interferometry of a nanomechanical resonator, Nature (London) **520**, 522 (2015).

[81] G. Zhao, Y. Wang, and X.-F. Qian, Driven dissipative quantum dynamics in a cavity magnon-polariton system, Phys. Rev. B **104**, 134423 (2021).

[82] M. P. da Silva, D. Bozyigit, A. Wallraff, and A. Blais, Schemes for the observation of photon correlation functions in circuit QED with linear detectors, Phys. Rev. A **82**, 043804 (2010).

[83] C. Lang, D. Bozyigit, C. Eichler, L. Steffen, J. M. Fink, A. A. Abdumalikov, Jr., M. Baur, S. Filipp, M. P. da Silva, A. Blais, and A. Wallraff, Observation of resonant photon blockade at microwave frequencies using correlation function measurements, Phys. Rev. Lett. **106**, 243601 (2011).

[84] F.-X. Sun, S.-S. Zheng, Y. Xiao, Q. Gong, Q. He, and K. Xia, Remote generation of magnon Schrödinger cat state via magnon-photon entanglement, Phys. Rev. Lett. **127**, 087203 (2021).

[85] D. Walls and G. Milburm, *Quantum Optics* (Springer, Berlin, 1994).

[86] M. O. Scully and M. S. Zubairy, *Quantum Optics* (Cambridge University, Cambridge, England, 1997).

[87] G. S. Agarwal, *Quantum Optics* (Cambridge University Press, Cambridge, UK, 2013).

[88] M. Fanaei, A. Foerster, H. A. M. Leymann, and J. Wiersig, Effect of direct dissipative coupling of two competing modes on intensity fluctuations in a quantum-dot-microcavity laser, Phys. Rev. A **94**, 043814 (2016).

[89] H. A. M. Leymann, C. Hopfmann, F. Albert, A. Foerster, M. Khanbekyan, C. Schneider, S. Höfling, A. Forchel, M. Kamp, J. Wiersig, and S. Reitzenstein, Intensity fluctuations in bimodal micropillar lasers enhanced by quantum-dot gain competition, Phys. Rev. A **87**, 053819 (2013).

[90] P. Rabl, Photon blockade effect in optomechanical systems, Phys. Rev. Lett. **107**, 063601 (2011).

[91] H. Fröhlich, Theory of the superconducting state. I. The ground state at the absolute zero of temperature, Phys. Rev. **79**, 845 (1950).

[92] S. Nakajima, Perturbation theory in statistical mechanics, Adv. Phys. **4**, 363 (1955).

[93] S. Li and A. Zhu, Perfect Single-magnon generator based on a hybrid cavity-magnonic system, Ann. Phys. **534**, 2100609 (2022).

[94] A. F. Kockum, A. Miranowicz, V. Macrì, S. Savasta, and F. Nori, Deterministic quantum nonlinear optics with single atoms and virtual photons, Phys. Rev. A **95**, 063849 (2017).

[95] O. Di Stefano, A. Settineri, V. Macrì, A. Ridolfo, R. Stassi, A. F. Kockum, S. Savasta, and F. Nori, Interaction of mechanical oscillators mediated by the exchange of virtual photon pairs, Phys. Rev. Lett. **122**, 030402 (2019).

[96] S. Filipp, M. Göppl, J. M. Fink, M. Baur, R. Bianchetti, L. Steffen, and A. Wallraff, Multimode mediated qubit-qubit coupling and dark-state symmetries in circuit quantum electrodynamics, Phys. Rev. A **83**, 063827 (2011).

[97] J. Majer, J. M. Chow, J. M. Gambetta, Jens Koch, B. R. Johnson, J. A. Schreier, L. Frunzio, D. I. Schuster, A. A. Houck, A. Wallraff, A. Blais, M. H. Devoret, S. M. Girvin, and R. J. Schoelkopf, Coupling superconducting qubits via a cavity bus, Nature (London) **449**, 443 (2007).